~~New method to determine~~ Determination of the ~~instrument spectral response function, applied to~~ TROPOMI-SWIR instrument spectral response function

Richard M. van Hees[1], Paul J. J. Tol[1], Sidney Cadot[1,2], Matthijs Krijger[1,3], Stefan T. Persijn[5], Tim A. van Kempen[1], Ralph Snel[1,4], Ilse Aben[1], and Ruud W. M. Hoogeveen[1]

[1]SRON Netherlands Institute for Space Research, Utrecht, the Netherlands
[2]Jigsaw B.V., Delft, the Netherlands
[3]Earth Space Solutions, Utrecht, the Netherlands
[4]Science and Technology B.V., Delft, the Netherlands
[5]VSL Dutch Metrology Institute, Delft, the Netherlands

Correspondence: Dr Richard van Hees (r.m.van.hees@sron.nl)

Abstract. The Tropospheric Monitoring Instrument (TROPOMI) is the single instrument on board of the ESA Copernicus Sentinel-5 Precursor satellite. TROPOMI is a nadir-viewing imaging spectrometer with bands in the ultraviolet and visible, the near infrared and the short-wave infrared (SWIR). An accurate instrument spectral response function (ISRF) is required in the SWIR band where absorption lines of CO, methane and water vapor overlap. ~~Therefore a novel method for ISRF determination for an imaging spectrometer was developed and applied to~~ In this paper, we report on the determination of the TROPOMI-SWIR ~~band. The ISRF of all detector pixels of the SWIR spectrometer has been measured during an~~ ISRF during an extensive on-ground calibration campaign. Measurements are taken with a monochromatic light source scanning the whole detector, using the spectrometer itself to determine the light intensity and wavelength. The accuracy of the ~~derived ISRF~~ resulting ISRF calibration key data is well within the requirement for ~~accurate~~ trace-gas retrievals. Long-term in-flight monitoring of ~~the ISRF is guaranteed by the presence of five SWIR~~ SWIR ISRF is achieved using five on-board diode lasers.

1 Introduction

The Tropospheric Monitoring Instrument (TROPOMI) is the single payload of the Copernicus Sentinel-5 Precursor (S5P) satellite mission~~(Veefkind et al., 2012)~~. The instrument maps the Earth's atmosphere ~~in two dimensions~~ using two spectrometer modules behind a common telescope, one covering the ultraviolet/visible (270–495 nm) and near-infrared (675–775 nm), and the other covering the short-wave infrared (SWIR) spectral range 2305–2385 nm. The ~~latter with a~~ spectral resolution of the SWIR spectrometer is about 0.25 nm ~~and~~ with a spectral sampling ~~distance of~~ interval of typically 0.1 nm. The TROPOMI instrument measures sunlight reflected by the surface and atmosphere of the Earth via the radiance port. Direct sunlight is measured via the irradiance port and internal diffuser for calibration purposes (Veefkind et al., 2012). The SWIR spectrometer (developed by SSTL, United Kingdom) consists of a slit, collimator mirror optics, an immersed grating ~~(developed by SRON, van Amerongen et al. (2012))~~(developed by SRON, van Amerongen et al., 2012), anamorphic prism and camera op-

tics consisting of multiple lenses, and a HgCdTe detector (developed by Sofradir, France). The detector has 1000 columns in the spectral dimension and 256 rows in the spatial dimension of which about ~~216 rows and 984 columns are nominally~~ 975 columns and 217 rows are illuminated.

The TROPOMI-SWIR band is used for the retrieval of ~~atmospheric CO and methane columns. The methane concentrations have to be measured with an accuracy of better than 1%. Therefore, the requirement on systematic errors is very strict~~the atmospheric trace gases carbonmonoxide, methane and water vapor. Simulations have shown that in particular the methane retrieval is very sensitive to errors in the instrument spectral response function (ISRF ~~), which is used to include the measured absorption line shapein the modeled Earth spectra (Hu et al., 2016). Therefore~~or instrument line shape). As a result, the requirement on the ISRF is formulated that it should be known with an accuracy of 1% of its maximum where the ISRF is greater than 1% of its maximum ~~(Buscaglione, 2011; Hu et al., 2016)~~(Hu et al., 2016). To reach the required accuracy, ~~the ISRF has~~ data have been measured with high spectral resolution ~~during on-ground calibration measurements~~ using a scanning monochromatic light source covering the SWIR band.

~~In the literature, the instrument spectral~~ For a comprehensive overview of various approaches applied to determine the ISRF for relevant past and future space-borne missions we refer to Sun et al. (2017). In summary, for the pioneering mission GOME on ESA's ERS-1 satellite and for the SCIAMACHY instrument on board ESA ENVISAT, no high-resolution ISRF was measured at all on ground. Information was derived from an on-board spectral light source with discrete line emissions (Schrijver et al., 2009). For the later OMI instrument on board NASA's EOS Aura satellite a white light source followed by a high-resolution monochromator was used to create a comb of narrow spectral lines (Dobber et al., 2006). A similar approach was followed for the other three bands of TROPOMI (Kleipool et al., 2018). The NASA OCO instruments had the ISRF measured with a monochromatic line source (Day et al., 2011; Sun et al., 2017).

Often no distinction is made between a *spread* function ~~(ISSF) and instrument spectral~~ and a *response* function~~(ISRF) are often confused~~. In this paper, ~~we define a "spread function" and a "response function"~~ the functions are defined as follows: a ~~"spread function "~~ spread function maps an object to image space, which involves many detector pixels; a ~~"response function "~~ response function maps an image to object space, which is a property of a given detector pixel. The ~~ISSF~~ instrument spectral *spread* function (ISSF) is measured simply by illuminating the spectrometer slit homogeneously with a monochromatic source and taking a detector image (frame). In the spectral dimension, about ~~4–5 points~~ 5 pixels have significant signal, as expected from the spectral oversampling. This is the spread function of the instrument for this wavelength. In Fig. 1b it is shown as a red cross section. When the wavelength is scanned in small steps over a set of frames, the signal in those frames for a given pixel ~~(that is illuminated in at least some of the frames)~~ forms an ISRF, with an arbitrarily fine sampling. This is shown as a green cross section in Fig. 1c. There is an infinite number of ISSFs (one at each wavelength) and a finite number of ISRFs (one for each pixel).

The ISSF consists of one sample from each ISRF of a few neighboring pixels on a row. If the ISRF varies negligibly between these pixels, the ISSF is a sparsely sampled version of this ISRF. ~~However, Fig.~~Figure 1a shows that the samples taken with increasing column index are ISRF points from the right side of the peak to the left side: the ISSF samples a mirrored ISRF, indicated by the light-green line ~~at bottom left~~in Fig. 1b.

~~During the~~ By design, the ISRF and dispersion of the TROPOMI instrument should vary only smoothly in the spectral and spatial dimension. This assumption will be validated in this study by determining the local ISRF for many pixels of the SWIR detector. The assumption is also used in the data analysis to interpolate the ISRF to pixels for which there are no reliable measurements and to reduce the effect of outliers.

The ISRF is determined from measurements using the radiance port and the irradiance port. Although differences between both data sets are not expected, they could not be ruled out. Light entering via the irradiance port follows a different path, via a diffuser.

The ISRF measurements are part of the on-ground ~~calibration measurements , the absolute wavelength of the source is not measured accurately enough~~calibration campaign performed at the Centre Spatial de Liège (CSL) in Belgium (Kleipool et al., 2018). The limited time slot did not allow to perform the measurements with a very accurate wavelength meter and wait for a stable laser at a given wavelength. Instead, the laser scanned slowly during data taking and each frame is ~~seen~~ treated as the measurement of an ISSF per row, ~~and~~ where the column index of the fitted center is used as a wavelength label for the row data. The ISRF of a pixel, based on data from a set of frames, is then the normalized signal as a function of wavelength in pixel units (non-integer values). It should not be confused with the ISSF, which has basically the same horizontal scale but then in integer pixel ~~values~~units. Only at the end of the algorithm is the ISRF of a given pixel converted to a function of wavelength in nm, using the wavelength assignment derived from an independent wavelength calibration measurement. This results in the ISRF calibration key data (CKD) which are used in trace-gas retrievals.

The measurements used for the ISRF characterization are presented in Sect. 2. A description of the method and algorithm used to derive the ISRF for all illuminated pixels is presented in Sect. 3. Details of the algorithm are discussed in Sect. 4, ~~where we also present the ISRF analysis~~ as well as the ISRF results based on the on-ground calibration measurements. ~~The validation of the irradiance ISRF using the radiance measurements is discussed at the end of~~ Comparison of the ISRF as determined from irradiance, radiance and on-board diode-laser measurements are discussed and the choice for the CKD is motivated. The validation of the SWIR ISRF is also part of the discussion (Sect. 4). The in-flight monitoring of the ISRF is briefly described in Sect. 5. This is followed by the conclusions in Sect. 6.

2 Calibration measurements

~~In this section, we describe the setup used during the ISRF calibration measurements, performed at the Centre Spatial de Liège (CSL) in Belgium, during the on-ground calibration campaign (Kleipool et al., 2018). In this setup, the~~

2.1 Measurements with the external laser

The light source employed in the ISRF characterization measurements is a 2 W continuous-wave optical parametric oscillator (OPO), custom-built by VSL (Delft, the Netherlands). The OPO is pumped by a single-frequency distributed feedback (DFB) fiber laser operating at 1064 nm which is amplified to 10 W by an ytterbium fiber amplifier. The OPO wavelength is set coarsely between 2290 nm and 2390 nm by manually setting the temperature of the periodically poled lithium niobate crystal

and rotating the etalon mounted on a galvo. The wavelength is scanned continuously over a range of about 2 nm by applying a changing piezo voltage to the fiber laser and simultaneously changing the crystal temperature with a predetermined dependence on the piezo voltage. ~~To avoid~~ The setup for the radiance and irradiance measurements is shown in Fig. 2.

During the radiance measurements, the power entering the instrument has been reduced with a neutral density filter, just after the OPO, to avoid saturation of the SWIR detector. To suppress speckle patterns on the detector, the light is sent to an integrating sphere via a high-speed spinning mirror with a small angle between the rotation axis and the normal. The light exits the integrating sphere and is collimated with a field stop and an off-axis parabolic mirror. The ~~instrument is mounted on a cradle in order to~~ beam corresponds to a swath-angle coverage of 1.1°, illuminating approximately 2 pixels in the swath direction. To scan all swath angles~~in a~~ , the instrument is mounted on a cradle. The automated wavelength scans were repeated 109 times to cover the range of 108° around nadir. ~~The beam corresponds to a swath-angle coverage of 1.1°, when the radiance port of TROPOMI is used. During irradiance ISRF measurements,~~ At each swath position, the wavelength was scanned in the opposite direction. The detector covers the wavelength range 2300–2389 nm, but due to time constraints, measurements have been collected of wavelengths between 2304 nm and 2386 nm, which covers the performance range 2305–2385 nm.

The field stop and parabolic mirror were replaced by a set of collimating lenses during the irradiance measurements, in which the whole swath is illuminated at once via the on-board solar diffuser. ~~With a neutral density filter just after the OPO, the power entering the instrument has been reduced to avoid saturation. During a wavelength scan , the~~ As there was no need to repeat measurements at different swath angles, each automated wavelength scan was repeated with increasing and decreasing wavelength scan direction. The irradiance data covers the full wavelength range.

Each automated wavelength scan of about 2 nm, or 20 spectral pixels, took about 165 seconds. The data is collected at 10 ~~Hzduring approximately 165 seconds, taking approximately~~ Hz, yielding 1650 ISSF samples in total and about 80 samples ~~. Background measurements are taken by closing a shutter between the filter and the spinning mirror. For more details on the setup, see Tol et al. (2018, Sect. 2).~~

~~Calibration measurementsvia the radiance port and irradiance port have been performed to verify that they are identical. The measurements of the radiance ISRF lasted significantly longer as not only the laser wavelength had to be scanned, but also the swath angle. Therefore,~~ per pixel. The laser scan speed was not constant, despite the small adjustments of the piezo voltage during the wavelength scan. Due to the large number of samples taken, this has no negative impact on the ISRF determination. During the measurements, a dedicated quick-look facility was available to monitor the conditions of the instrument and to show the measured signals in real-time. A wavelength meter was used by the operators to set the start wavelength of each automated wavelength scan. The operators kept a log during the measurement campaign to reported on issues during the measurements. Overall, more problems were reported during the radiance ~~ISRF measurementsabout 100 wavelength scans per manual wavelength setting are performed to cover all swath angles, and due to time constraints one-way wavelength scans were taken. During the irradiance ISRF measurements each wavelength scan was performed up and down~~measurements, mostly due to instability of the source due to drift and mode hopping. Detailed data analysis was performed after the measurement campaign was finalized, denying the possibility to improve or redo certain measurements.

3 Methodology

In this section, we describe our method to characterize the TROPOMI-SWIR ISRF in general. Specific measurement issues will be discussed in Sect. 4.

2.1 ISRF shape

To derive the ISRF from the measured ISSF, an assumption has to be made on the shape of the ISRF. In an iterative way, the ISRF shape can be made more complex to fit its detailed features. At the start of the procedure it is assumed that the ISRF is just a convolution of a block distribution with a normal distribution. This corresponds to an image of the slit on the detector (the block), with the optics blurring the image (the normal distribution). In later iterations, the normal distribution is allowed to be skewed. As the measurements show longer spectral tails, a dedicated tail function is added to the ISRF to account for this. For the tails, several functions were tried. In the end, the Pearson type VII distribution resulted in the best fit.

Mathematically, the ISRF is modeled by the weighted sum of functions for the peak and the tails. Peak function $\mathcal{S}$ is a skew-normal distribution convolved with a block distribution and tail function $\mathcal{P}_7$ is a Pearson type VII distribution.

$$\mathcal{R}(c;d,s,w,\eta,\gamma,m,c_0) = \begin{array}{l}(1-\eta)\,\mathcal{S}(c;d,s,w,c_0)\\ +\eta\,\mathcal{P}_7(c;\gamma,m,c_0)\end{array}$$

The two constituent distributions have been normalized to area 1, so that weight η is the fraction of the total area in the tail function. The weight has to be in the range $0 \le \eta \le 1$. The ISRF model is a function of column index c with its mean at c_0, where both are non-integer numbers.The wavelength assignment is performed when the ISRF calibration key data (CKD) are generated: the SWIR wavelength calibration key data are used to assign a wavelength to the center of a pixel and the ISRF is defined relative to that wavelength.

Peak function $\mathcal{S}$ has three shape parameters, the skew-normal width d, skewness parameter s and block width w:

$$\mathcal{S}(c;d,s,w,c_0) = \begin{array}{l}\frac{\mathrm{erf}\left(\xi_+/\sqrt{2}\right)-\mathrm{erf}\left(\xi_-/\sqrt{2}\right)}{2w}\\ -2\frac{T(\xi_+,s)-T(\xi_-,s)}{w}\end{array}$$

with

$$\xi_\pm = \frac{\sqrt{1-\delta^2}}{d}(c-c_0\pm\tfrac{w}{2})+\delta \quad \text{where} \quad \delta = \frac{\sqrt{2}\,s}{\sqrt{\pi(1+s^2)}}$$

and using Owen's T function (Patefield and Tandy, 2000)

$$T(z,s) = \frac{1}{2\pi}\int_0^s \frac{\exp\left(-\frac{1}{2}z^2(1+t^2)\right)}{1+t^2}\,\mathrm{d}t.$$

~~Tail function $\mathcal{P}_7$ has two shape parameters, γ and m:~~

$$\mathcal{P}_7(c;\gamma,m,c_0) = \frac{\Gamma(m)}{\gamma\sqrt{\pi}\Gamma(m-\frac{1}{2})}\left(1+\frac{(c-c_0)^2}{\gamma^2}\right)^{-m}$$

~~with $m > 1/2$ and $\gamma > 0$. The specific case $\mathcal{P}_7(c;\gamma,1,c_0)$ is the Lorentz distribution with half width at half-maximum γ.~~

2.1 Measurements with the on-board diode-lasers

TROPOMI's on-board calibration system includes five distributed feedback lasers (Nanoplus, Germany) to monitor stray light and ISRF (Veefkind et al., 2012). The wavelength is scanned by tuning the temperature of each laser using the thermo-electric cooler integrated in the laser housing. These diode lasers are tuneable over a range of 7 nm (about 70 pixels), but due to operational constraints monitoring is restricted to 0.6 nm (about 6 pixels). Analysis revealed that the lasers are very stable and can perform very precise wavelength scans are scanned in 430 seconds, taking over 700 samples per pixel (at 10 Hz). The distribution of the five lasers is listed by their operational wavelength (at the center of the scan) and corresponding pixel (between brackets): 2311.8 nm (154), 2328.2 nm (341), 2340.0 nm (471), 2357.5 nm (659) and 2372.2 nm (813). The lasers illuminate the SWIR spectrometer via a dedicated diffuser. The speckle in the laser signal can be suppressed by oscillation of the diffuser around the nominal angle. However, as the diffuser mechanism is a life-limited item, only during the on-ground calibration campaign and during the in-flight commissioning phase, measurements will be performed with a moving diffuser.

2.2 Data preparation

~~The measurement data are corrected for background, pixel response~~ The three measurement data sets (irradiance, radiance and diode-lasers) are corrected for detector features such as memory and pixel response non-uniformity ~~and stray light(irradiance only). Absolute (ir)radiance calibration is not required. Readouts from bad pixels are discarded in~~ (PRNU), using the operational level-1b processor developed by KNMI (Kleipool et al., 2018). Changes of the background signal are removed by dedicated background measurements, which include offset, detector dark current and thermal background signal. These measurements are performed regularly during the measurements with the external laser, by blocking its signal with a shutter (Fig.2). For the on-board lasers the background signal is measured before and after each wavelength scan. A non-linearity correction is not implemented in the operational processor. It is also not needed for the ISRF characterization, as the error is small: detector non-linearity was measured to be about 0.1% to 0.2% (Hoogeveen et al., 2013). In irradiance measurements, where the light is imaged as a vertical line, the ISRF at one row could be affected by stray light from other rows. Hence, these data are corrected for stray light using the operational processor. In radiance measurements, where the light is imaged as a spot, there is no stray light from other rows and the stray-light correction is not applied. The diode laser measurements are also not corrected for stray light, as they are intended to monitor stability.

Calibration key data for pixel quality have been derived from on-ground measurements. The pixel quality is based on several tests to identify pixels with too high dark current or noise. Most of the pixels with low quality exhibit high noise. About 260 pixels with a very low pixel quality ("bad pixels") are rejected from the analysis.

~~The measurement data of each wavelength scan are processed separately. Frames where the light source was off or very weak are discarded. In each remaining frame, the column with the maximum average signal is determined and the columns up to 7 pixels from this peak column are selected, to include the faint signal of the tails~~During data analysis it was found that a significant amount of irradiance measurements had to be rejected from the analysis due to detector saturation, as a result of an unexpectedly large variation of the laser intensity. From the radiance measurements partly illuminated rows were rejected.

3 Methodology

In this section, the method is described to determine the TROPOMI-SWIR ISRF from the on-ground measurements presented in the previous section. A general description is given first, followed by the details of the method.

3.1 ~~ISSF fit~~

~~The ISRF parameters cannot be retrieved directly from the measurements, because~~ The first step in the analysis is to obtain the wavelength and intensity of the signal ~~are unknown and have to be determined via the ISSF. The ISSF is assumed to be the mirrored version of an ISRF, which can be modeled with the function $A\mathcal{R}(c; d, -s, w, \eta, \gamma, m, c_0)$ using Eq. (13); only its skew parameter s has the opposite sign. In each frame, the ISSF of an illuminated row is fitted to the ISRF shape to normalize the signals and to find the wavelength peak position expressed in pixel units (Fig. 1b). The normalized signal and the distance to the fitted peak position yields one point~~ for each frame measured in each wavelength scan. As a first approximation, the ISSF shape corresponds to an image of the slit on the detector with the optics blurring the image. The mathematical model for the ISSF at this stage is a convolution of a normal distribution and a uniform distribution. Non-linear least squares minimalization is used to fit this function to the data. As a result, a wavelength can be assigned to each measurement and the signals can be normalized by the fitted signal intensity. The wavelength is expressed as a non-integer column distance. The wavelength assignment in nm is performed in the final step of the ISRF ~~shape, illustrated by the intersection of the red and green line in Fig. 1a. The normalized signal~~ determination.

The shape of an ISRF at location (r, c), where r is along the spatial dimension and c along the spectral dimension, is given by the normalized signal measured by detector pixel (r, c) as a function of ~~the fitted peak position forms a set of points covering the ISRF shape (Fig. 1c).~~

3.1 ~~ISRF fit~~

~~For a specific pixel in a row, each frame yields one ISSF fit and thus one point of the ISRF shape. While scanning the laser and recording frames, the set of points covering the ISRF shape of a given pixel is generated from the ISSF fits. As the laser-wavelength scan is not regular, the ISRF data pointsare not on a regular grid. Therefore, the~~ wavelength. Typical examples of ISRFs obtained from resp. irradiance, radiance and diode-laser measurements are presented in Figs. 3–5, taken across the SWIR detector from top left to bottom right. The locations vary slightly between the measurement types to avoid measurements affected by strong saturation effects or laser instabilities. In the upper panels, the ISRF data points are shown as black dots.

The irregular distances between the dots clearly show that the scan speed of the external laser is not constant, as explained in Sect. 2.1. This has no negative effect on the curve fitted through the data points~~in the scan range are collected in bins of 1/32 of a spectral pixel and a median is applied to the data points in each bin. Empty bins are discarded. Reducing the number of points like this also speeds up the fitting and reduces noise while no significant details arelost. The ISRF is fitted with the function $AR(c; d, s, w, \eta, \gamma, m, c_0)$ using Eq. (13).~~

~~The quality of the fit is determined by calculating the fit variance, the sum of the squared fit residuals where the fit function is larger than 6% of the maximum, divided by the number of degrees of freedom (number of points minus the free fit parameters). The square root of the fit variance is the rms value~~. Furthermore, the fit is also quite robust against single outliers and missing data points. The peak width due to the projection of the slit on the detector is constant when expressed as a wavelength interval, but expressed as a column distance it decreases towards larger columns (longer wavelengths), because the spectral dispersion changes. The peak height increases to keep an integrated area of 1. The ISRF in the panels (a_1) and (a_2) are clearly skewed, while the other three are, by eye, symmetrical. The signal-to-noise in all three measurements is sufficient to determine the signal accurately up to 4.5 pixels from the center. In the calibration key data the ISRF will be defined in this range only. The ISRF outside this range will be set to zero. Any remaining signal is considered as stray light, in line with the stray-light correction algorithm (Tol et al., 2018).

3.1 ~~ISRF parameter smoothing~~

~~The ISRF calibration key data has to be valid for the whole SWIR spectral range and for all swath angles~~The one-step approach described so far would actually result in ISRF fit residuals much larger than shown in Figs. 3–5. The residuals would show systematic oscillations with a period of one pixel. These occur when a simplified model is applied to a poorly sampled ISSF, leading to errors depending on whether the peak is at a measured point or between two measured points (see Fig. 1b). In addition, the residuals of an asymmetric ISRF would show significant left-right differences, mostly negative residuals to the left and positive residuals to the right, when a symmetric model is used in the ISSF fit.

A TROPOMI-SWIR ISSF measurement has typically 5 spectral pixels with sufficient signal-to-noise, not enough to fit all parameters of the complete ISRF model including a description for skewness and tails. However, the ISRF ~~fits are valid locally (at location (r, c)) and not available for all pixels. It is expected that the fit parameters that define the local ISRF vary only smoothly over the surface of the detector as this is determined by the spectrometer optics. Therefore, a bivariate polynomial fitting is used to smooth and to interpolate the ISRF fit parameters. The model with variables r and c, where the first row and column are mapped to -1 and the last row and column mapped to $+1$, is given by~~

$$E_{\text{fit}}[r, c; \boldsymbol{a}] = \sum_{k=0}^{M(M+3)/2} a_k T_{m-n}\left(2\frac{r}{255} - 1\right) T_n\left(2\frac{c}{999} - 1\right),$$

~~using Chebyshev polynomials of the first kind $T_n(x)$ and indices~~

$$m = \left\lfloor \tfrac{1}{2}\left(\sqrt{1+8k}-1\right)\right\rfloor,$$

$$n = k - m(m+1)/2.$$

derived with the approach so far is closer to the true ISRF than the simplified model used for the first ISSF fit. Using the mirrored shape of the ISRF at a given detector location as the shape of the ISSF at that location, the ISSF is fitted again to yield an updated wavelength and intensity as input to the determination of the ISRF (Sect. 3.2). The residuals of the resulting ISRF fit are much smaller. This procedure should be repeated until the residuals are no longer improving.

~~To obtain good results~~

So far, a general approach is presented to determine high-resolution ISRFs for a spectrometer that measures the ISSF with only a few spectral pixels, using a scanning monochromatic light source. Essential is to use the instrument itself to determine the wavelength and intensity of the light. This method enables the necessary measurements to be taken within reasonable time (days) even for detectors with more than 100,000 pixels. Next, a model is defined for the TROPOMI-SWIR ISRF and a practical implementation is shown of the iterative approach.

3.1 ISRF model

The mathematical model for the ISRF ~~parameter fitting, obvious outliers in the individual ISRF-fit results should be rejected before the bivariate polynomial fit is performed. Given the distribution of outliers (in columns at the same wavelength), it is judged that most of them are caused by laser artifacts. The following data selection was applied before the parameter fitting: no ISRF fit is performed on the first and last two pixels of an automated scan, because the whole peak of the ISRF should be present in the data; curve fit solutions were rejected in case the curve-fitting routine signaled an error. This happened for a small fraction of the pixels ($< 1\%$) , due to bad ISRF data; unrealistic curve-fit solutions are rejected:~~ should be flexible enough to represent the range of ISRF shapes adequately with the smallest number of parameters. The TROPOMI-SWIR ISRF is modeled by the weighted sum of functions for the peak and the tails. The peak function is a skew-normal ~~width $d < 0.1$ or skew $|s| > 5$; poor fits are rejected based on their rms value. Irradiance measurements: reject data of the whole column when its median rms is larger than 0.0065. Radiance measurements: reject ISRF fits with an rms larger than 0.0065. The ISRF of a given pixel can sometimes be derived multiple times, because (*i*) the automated scans overlap in wavelength; (*ii*)for irradiance measurements, all automated scans are performed twice: scanning up and down in wavelength.~~ distribution convolved with a uniform distribution. This corresponds to a (~~*iii*) for radiance measurements, successive scans overlap in~~ possibly asymmetric) image of the slit on the detector, with the optics blurring the image. Beirle et al. (2017) use an asymmetric version of the ~~swath direction by half a pixel~~exponential power distribution ('Super Gaussian'). This function is computationally less demanding and suitable for general ISRF simulations, but in our case the fit residuals are larger than with the convolution above. For the ~~parameter fits, only the ISRF fit with the smallest rms is used.~~ tails a function is needed with an adjustable tail weight. A suitable function is found to be the Pearson type VII distribution, which is a generalization of the Gauss and Lorentz distributions. It can represent the wings of SWIR spectral stray light satisfactorily (see Tol et al., 2018, Fig. 9).

~~Orders M of the bivariate Chebyshev expansions applied to the irradiance and radiance data are equal, except in cases~~ The normal distribution with mean 0 and standard deviation σ is given by

$$\mathcal{G}(c;\sigma) = \frac{1}{\sigma\sqrt{2\pi}} \exp\left(-\frac{c^2}{2\sigma^2}\right). \tag{1}$$

The skew-normal distribution is a generalization including an extra skewness parameter s:

$$\mathcal{N}_1(c;\sigma,s) = \left[1 + \operatorname{erf}\left(\frac{s\,c}{\sigma\sqrt{2}}\right)\right] \mathcal{G}(c;\sigma). \tag{2}$$

This function has mean $\sigma\,\delta$ and standard deviation

$$d = \sigma\sqrt{1-\delta^2}, \tag{3}$$

with

$$\delta = \frac{\sqrt{2}\,s}{\sqrt{\pi(1+s^2)}}. \tag{4}$$

To interpret fitting results more easily, the skew-normal distribution is written in terms of d instead of σ and a parameter c_0 is included for the mean:

$$\mathcal{N}_2(c;d,s,c_0) = \mathcal{N}_1\left(c - c_0 + \frac{d\,\delta}{\sqrt{1-\delta^2}}; \frac{d}{\sqrt{1-\delta^2}}, s\right) \tag{5}$$

$$= \frac{\sqrt{\frac{1}{2}\pi + \frac{1}{1+s^2} - 1}}{\pi d}\left[1 + \operatorname{erf}\left(\frac{s\,\xi_0}{\sqrt{2}}\right)\right] \exp\left(-\tfrac{1}{2}\xi_0^2\right), \tag{6}$$

with

$$\xi_0 = \frac{\sqrt{1-\delta^2}}{d}(c - c_0) + \delta. \tag{7}$$

Peak function $\mathcal{S}$ is the convolution of skew-normal distribution $\mathcal{N}_2(c;d,s,c_0)$ and a uniform distribution with mean 0 and full width w (the 'block width'):

$$\mathcal{S}(c;d,s,w,c_0) = \frac{1}{w}\int_{c-w/2}^{c+w/2} \mathcal{N}_2(u;d,s,c_0)\,\mathrm{d}u. \tag{8}$$

This can be written as

$$\mathcal{S}(c;d,s,w,c_0) = \frac{\operatorname{erf}\left(\xi_+/\sqrt{2}\right) - \operatorname{erf}\left(\xi_-/\sqrt{2}\right)}{2w} - 2\frac{T(\xi_+,s) - T(\xi_-,s)}{w} \tag{9}$$

with

$$\xi_{\pm} = \frac{\sqrt{1-\delta^2}}{d}(c - c_0 \pm \tfrac{w}{2}) + \delta \tag{10}$$

and using Owen's T function (Patefield and Tandy, 2000)

$$T(z,s) = \frac{1}{2\pi}\int_0^s \frac{\exp\left(-\frac{1}{2}z^2(1+t^2)\right)}{1+t^2}\,\mathrm{d}t. \tag{11}$$

Tail function $\mathcal{P}_7$ is the Pearson type VII distribution

$$\mathcal{P}_7(c;\gamma,m,c_0) = \frac{\Gamma(m)}{\gamma\sqrt{\pi}\Gamma(m-\frac{1}{2})}\left(1 + \frac{(c-c_0)^2}{\gamma^2}\right)^{-m} \tag{12}$$

with $m > 1/2$ and $\gamma > 0$. This distribution is a generalization of the Lorentz distribution where the tail shape can be changed; the specific case $\mathcal{P}_7(c;\gamma,1,c_0)$ is the Lorentz distribution with half width at half-maximum γ. ISRF function $\mathcal{R}(c;d,s,w,\eta,\gamma,m,c_0)$ consists of a peak function with three shape parameters d, s ~~. The irradiance data has a better coverage in both spectral and spatial directions, so a higher order $M = 7$ could be applied on the parameters d and s, which show much more structure than the other fit parameters. An order $M = 6$ was used on the radiance data. Order M used for~~ and w, and a tail function with two shape parameters γ and ~~η are 5, 2 and 2, respectively. The result of this step yields the~~ m:

$$\begin{aligned}\mathcal{R}(c;d,s,w,\eta,\gamma,m,c_0) =& (1-\eta)\mathcal{S}(c;d,s,w,c_0)\\ &+\eta\mathcal{P}_7(c;\gamma,m,c_0).\end{aligned} \tag{13}$$

The mean is at c_0, the integral is 1 and the integral over the tail part only is η.

The requirement on the TROPOMI-SWIR ISRF states that the ISRF ~~parameter models that are employed to calculate the ISRF calibration key data for each and every pixel. These key data are used in the SWIR retrieval algorithms that derive the gas columns.~~

~~The quality of~~ should be known with an accuracy of 1% of its maximum. A stringent implementation of the requirement would be that the ~~parameter fitting is determined by comparing the measured~~ absolute value of all residuals should be less than 1% of the maximum of the ISRF (about 0.004), but that leaves no room for outliers. An alternative measure of the fit quality turns out to be an rms value calculated as the square root of the sum of the squared difference between the ISRF fit residuals, using points where the fit function is larger than 6% of its maximum, divided by the number of ISRF data points ~~with the ISRF that results from the parameter model. An $\mathrm{rms}_{\mathrm{model}}$ value is determined in a similar way as the rms defined in Sect. **??**. In general, the parameter smoothing will result in better and smoother ISRF calibration key data due to averaging and interpolation. Possibly counter intuitive, the rms value will be slightly larger as the ISRF data points are now compared with a smoothed ISRF instead of an optimized local ISRF that might be influenced by measurement imperfections~~minus the number of free fit parameters. The threshold of 6% is arbitrary, but a lower value would include more of the tails where the residuals

are always very small, which would make this measure less sensitive. The advantage of this measure is that it is less sensitive to small outliers, and sensitive to large outliers which can corrupt the fit procedure. Therefore, we use this rms as a measure of the fit quality.

3.2 ISRF parameter iteration

An ISSF has typically only 4-5 spectral pixels with sufficient signal-to-noise ratio. Therefore, only fitting with a few parameters is accurate, yielding significant errors in the resulting ISRF. An iterative approach has been developed, starting with a symmetric model without tails. Once the ISRF has been fitted, the skew and tails are known approximately, and can be included as fixed properties while the ISSF is fitted again. The ISRFfit also benefits from a reduction of the number of parameters. Therefore, the refitted block width as a function of row and column is smoothed and used as a fixed property in the final ISRFfit. In the end, the ISSF and ISRF are determined in four passes or 'stages'. The differences between the parameter fitting in ISSF In the iterative approach as introduced above we start with a simplified model for the ISSF to determine the central wavelength and intensity of the laser. Many ISSF fits are used to estimate the (local) ISRF, so the ISRF can be determined with many parameters. For the next iterations we use the fact that the ISSF is equal to the mirrored local ISRF, and ISRF fits in the different stages are summarized in Table **??**the only free parameters in the successive iterations in the ISSF fit are the wavelength and the intensity.

The procedure and number of stages This procedure and the number of iterations have been verified using synthetic ISRF data. To illustrate the ISRF parameter iteration, we present the results of simulations using two realistic ISRFs, one nearly-symmetric and the other skewed. The calculations are performed without noise, and the ISRF is kept constant in each data set. A simulated measurement data set was constructed given the shape of About 2000 synthetic ISRFs have been constructed using the ISRF model (Eq. 13) and combinations of the 7 parameters covering most of the ISRF and assuming a laser scanning over about 20 spectral pixels in small steps (100 per spectral pixel) similar to the actual calibration measurements. Table 1 lists the intermediate results of the ISRF fit at the end of each stage, while Fig. **??** shows the parameter space. This data set has been generated with and without realistic noise. The simulations confirmed our guess that not all ISRF parameters can be fitted at the same time, because the tail parameters γ and m are not independent and the fit of these parameters is further complicated by the small signal of the tails. In early computations to determine the TROPOMI-SWIR ISRF, the tail parameter m was fixed to 1.2, based on the shape of the tails found in stray-light measurements. The simulations with synthetic data shows it is better not to fix m, because its true value is poorly known and it improves the convergence of the ISRF model towards the true ISRF.

The ISRF parameters of the skewed model are derived with high accuracy (better than 0.5%) after 3 stages. In contrast, other parameters. The best convergence towards the true ISRF, both in speed and in accuracy, is achieved by fixing peak width parameter w. However, in this case w needs to be known better than 1%, which is unrealistic. Second best is to fix tail fraction η. The tail fraction is nearly constant across the detector and from detailed analysis of the ISRF determined after the first iteration its value is usually be between 0.1 and 0.12. Therefore, assuming a tail fraction of 0.11 would work for most ISRF fitting. To overcome problems in case the parameter iteration has problems deriving the ISRF tail parametersfor the nearly symmetric ISRF, where the tail width is overestimated by more than 20%and the tail fraction is underestimated by 25%. The

curve-fitting routine is not the problem, because Fig. **??**c shows that the fit residuals are almost zero after stage 3. Apparently, in the case of a symmetric function the algorithm converges to a sub-optimal solution. In this case the algorithm has difficulty separating the nearly symmetric peak from the also symmetric tail function. However, true tail fraction is outside this range, the ISRF fit is performed twice. First only fixing the tail fraction (from the previous iteration), then only fixing w (improved guess from the previous ISRF fit). We refer to each repeated step of the method as "stages", because each step contains several computations: one ISSF fit and two ISRF fits.

This approach generates consistent good results after 4 stages. Synthetic data show that the differences between the true determined ISRF and the derived ISRF are less than 0.25% and are considered acceptable. The algorithm converges in two stages, see Fig. **??**b and **??**d. Any further iterations will only marginally improve the results. This is true for noiseless synthetic data, and it should be noted that performing stage 3 does improve the derived ISRF parameters of real measurements. Stage 4 is added because the block width is fixed to its model (derived in the previous stage) in the ISRF fit. This turns out to reduce the variance in the tail parameters significantlytrue ISRF are within 0.0005 (about 0.125% of the ISRF maximum). Adding realistic noise has a very minor effect, due to the large number of measured ISSF samples: the residuals are doubled and the determined ISRF is more slightly symmetrical. Because the true ISRF is generated with the same ISRF model used for the fit, one would expect that the determined ISRF matches the true ISRF perfectly. However, this is not the case due to the fact that details of the true ISRF are lost in the fit of the poorly sampled ISSF. According to an extra simulation, the determined ISRF matches the true ISRF nearly perfectly when the ISSF signal is measured with 10 instead of 5 spectral pixels.

4 Discussion of results

Typical examples of various shapes of the TROPOMI-SWIR ISRF are The convergence of the method is illustrated in Fig. **??** (irradiance measurements) and Fig. **??** (radiance measurements). Shown are the stage 4 results of the ISRF for five columns: 128, 300, 5406, where the ISRF shapes presented in Figs. 3–5 are simulated. For all five simulated ISRFs a quick convergence is achieved. The large residuals between the asymmetric ISRF after stage 1 and true ISRF are due to a shift in the peak position, while the shape of the final ISRF agrees with the true ISRF, 726 and 935, respectively. A median has been taken over all rows illuminated. From visual inspection of the displayed ISRFs, one can conclude that: (*i*) the ISRF is sharper and higher at higher column number (longer wavelength); (*ii*) the ISRF fit resembles the ISRF data very well, e. g. the residuals are very small, except where small artifacts can be identified see Table 1.

3.1 ISRF parameter smoothing

The goal of the on-ground calibration is to determine the SWIR ISRF for all pixels, because trace-gas retrieval needs the ISRF for the whole SWIR spectral range and for all swath angles. However, the ISRF could not be measured for all pixels due to measurements with too strong laser signal (rejected before analysis), bad pixels and laser instability. Therefore, it is necessary to interpolate the local ISRFs. Minor problems with the OPO are still present in the ISRF data ; (*iii*)the fit residuals of the irradiance ISRF are nearly a factor 2 smaller compared with the radiance ISRF.

~~The Pearson VII distribution has two parametersto control its shape: m and γ. When both are free parameters, the median value of m in the successful ISRF fits is 1.65 for radiance measurements and 1.25 for irradiance measurements. The difference is likely due to differences in stray light in these measurements. In all subsequent fitting, shape parameter m is fixed to 1.25 to enhance convergence of the curve-fitting routine and inter-comparison between ISRFs derived from irradiance and radiance measurements. It has to be noted that the contribution of~~ points (see Figs. 3–5), which may affect the ISRF fit yielding minor deviations of the fit parameters. Assuming that these deviations are random and that the shape of the ~~tail to~~ ISRF varies only smoothly over the surface of the detector (as it is determined by the spectrometer optics), then the quality of the ISRF would benefit when the ISRF parameters are smoothed and interpolated using bivariate polynomial fitting. Any high-frequency detector features still present in the data due to imperfect calibration or local changes in the detector PSF should then be visible in the ~~ISRF is small ($\leq 10\,\%$) and only significant 1-2 pixels away from the peak. It has been verified that fixing the m parameter has negligible effect on the resulting ISRF and the fit residuals expressed in the rms value~~difference between the local and smoothed parameter values.

The selected bivariate polynomial fit uses Chebyshev polynomials of the first kind T_n to minimizes the problem of Runge's phenomenon. The model at a location specified by row r and column c, where the first row and column are mapped to -1 and the last row and column are mapped to $+1$ is given by

$$E_{\text{fit}}[r, c; \boldsymbol{a}] = \sum_{m=0}^{M} \sum_{n=0}^{m} a_{mn}\, T_{m-n}\left(2\frac{r}{n_{\text{row}}-1} - 1\right) T_n\left(2\frac{c}{n_{\text{col}}-1} - 1\right), \tag{14}$$

where $n_{\text{row}} = 256$ and $n_{\text{col}} = 1000$ for the SWIR detector. The order M is the maximum of the sum of the exponents.

~~Table ?? summarizes the irradiance ISRF characterization. The number of good fits increases with every stage, except for the final stage where, in the ISRF fit~~The bivariate polynomial fitting is sensitive to obvious outliers. Therefore, ISRF fits have been rejected when the fit quality is low: rms > 0.003, skew parameter $|s| > 5$, tail parameter γ is outside the range $[0, 3]$ or tail parameter m is outside the range $[0.5, 3]$. The order M of the bivariate polynomial fit is optimized for each ISRF parameter to minimize the variance of the difference between the raw values and the fitted value. An order $M = 6$ is used for skew parameter s, ~~the block width is fixed to the value obtained in the previous stage. The goal of this final stage is , instead, to increase the quality of the tail fitting. This indeed happens as the standard deviation in the tail parameters is reduced by 30–50 %~~$M = 4$ for peak parameters d and w, and $M = 2$ for tail parameters γ and m.

The ~~final results of the irradiance ISRF are presented in the appendix of this article, shown are~~ smoothed ISRF parameters are employed to calculate the ISRF calibration key data for each and every pixel. Residuals are examined to check whether the excluded local variations are small enough to ignore. Actually, the smoothed ISRF parameters are calculated at the end of each stage, because the ISSF fit of the next stage, in general, benefits when erroneous ISRF fit results are not propagated to the next stage.

4 Discussion of results

Of the 2000 simulations with synthetic data performed, the ~~value of each ISRF parameters from the ISRF fit and after the bivariate polynomial fitting, see Figs. 9~~results of those that closely resemble the measured ISRF examples as shown in Figs. 3~~??~~. ~~As an example, the skew-normal width is shown in : Fig. 8a its fitted value, Fig. 8c the bivariate polynomial fit result, and in Fig. 8b the difference between the two. The stripe pattern in Fig. 8a is due to scanning imperfections of the laser. They are removed and interpolated in Fig. 8c, but reappear in the difference plot of~~ 5 will be used for illustration. The convergence towards a true ISRF from synthetic measurements is presented in Fig. ~~8b. Conclusions for all fitting parameters are :Block width w of the ISRF is determined by the projection of the slit onto the detector and therefore decreases as a function of wavelength~~6. These simulations are performed with an ideal laser: constant wavelength scan speed (using the average 0.00125 nm/s from the measurements) and constant laser signal. As expected, ~~no variation is seen over the spatial dimension of the detector (swath angle). Skew-normal width d shows more fine-scale structure than the other parameters. The pattern is probably due to variations in the sensitive area of the detector as the pattern is also seen in sensitivity plots of the detector alone (Hoogeveen et al., 2013). The fine-scale structures are smoothed in the parameter fit. This only has a minor effect on the quality of the ISRF calibration key data, as will be discussed later in this section. Skew parameter s shows that~~ the fit residual and the deviation from the true ISRF is still significant after the first stage, but the procedure quickly converges in subsequent stages. The final residuals and differences with respect to the true ISRF are much smaller than the requirement on the ISRF ~~is positively skewed ($s > 2$) at shorter wavelengths, and negatively skewed at longer wavelengths, but with a gradient along the swath. It appears the algorithm excludes s values between -0.6 and $+0.6$ as the difference between these curves is only very small ($< 10^{-3}$) . The parameter fit of s will interpolate this gap, introducing an error in the parameter s. However, width parameter d has been designed such that no errors are introduced by the ISRF parameter fit . Tail parameters η~~ knowledge. Table 1 shows that all ISRF parameters converge towards their true values during the ISRF parameter iteration.

The local ISRFs determined from irradiance measurements (Fig. 3c) and ~~γ show little variation over the swath, but their values can vary greatly from one column to the next. The tails have a low signal (< 0.01) outside the peak (see Figs. ?? and ??) . The low signal hampers the least-square minimization algorithm, leading to significant variation in the tail parameters. The bivariate fitting reduces the variation over swath and wavelengths.~~ radiance measurements (Fig. 4c) have typical fit residuals smaller then 0.004, except for a few outliers. These outliers correspond with the presence of (small irregular) wavelength jumps during the measurements. Some of the fit residuals show systematic features, but they are not consistent between both datasets. Therefore, the ISRF model (Eq. 13) is considered a good representation of the ISRF shape. The fit residuals determined from the on-board diode-laser measurements (Fig. 5c) are less noisy, because the speed of the wavelength scan was much lower and the diode lasers were better behaved.

~~Figure ??a shows the color-coded rms~~

Several fit thresholds are introduced in section 3.1, to optimize the bivariate polynomial fitting of the ISRF ~~fits. The pixels classified as good, i. e. meeting the requirement for ISRF knowledge, have an rms residual smaller than 0.004,equal to 1~~parameters. Low quality fits are identified by a high rms value. The median rms value is about 0.0017 for irradiance measurements, hence a reasonable threshold value is set at 0.003. Saturated measurements are rejected from analysis, but some

ISRF fits are still affected by nearby saturation. Therefore, ISRF fits with an exceptionally large skew-normal width value are rejected.

Of 211,575 pixels of the SWIR detector in the operational wavelength and swath ranges, we have ISRF data measured through the irradiance port of 195,892 pixels. For 7 % of the ~~maximum value of the ISRF. The bands with bad or moderate fits are attributed to laser artifacts,except for the columns at both ends, which are not scanned by the laser. The little spots of just a few pixels are caused by bad pixels. The quality of the ISRF fits as determined with the parameters from the bivariate parameter-fitting models~~ pixels ISRF data was not available or rejected due to possible saturation. The ISRF parameter smoothing at the end of stage 1 is based on about 116,000 local ISRF, because 73,616 ISRF fits were rejected due to the rms condition and about 6000 due to too large skew and skew-normal width. The number of used ISRF fits increased per stage to about 164,000 at stage 4, with only 28,900 rejected due to the rms condition and about 2,400 due to too large skew and skew-normal width. The rms values of the irradiance ISRF are shown in Fig. ~~??b. Here the regions with moderate or bad quality fits are extensions of moderate and bad regions in Fig. ??a. There are a few small regions which coincide with the fine-scale structures visible in the~~ 7a.

The number for the radiance measurements are significantly lower: ISRF data is available for 150,000 pixels. For 30 % of the pixels ISRF data was not available or rejected due to partial illumination of the pixels by the laser spot. The ISRF parameter smoothing at the end of stage 1 is based on about 63,000 local ISRFs, because 84,300 ISRF fits were rejected due to the rms condition and about 3000 due to too large skew and skew-normal width. The number of used ISRF fits increased per stage to about 92,500 at stage 4, with only 51,~~see for example around row 50 at columns 525 and 610. However, regions with good quality ISRF parameter fits are distributed over the entire array,and the~~ 300 rejected due to the rms condition and about 2,000 due to too large skew and skew-normal width. The rms values of the ~~ISRF parameters in these regions are consistent with the overall trend.This gives us confidence that our SWIR ISRF characterization is successful, and within the requirement on the knowledge of the ISRF .~~ radiance ISRF are shown in Fig. 7b.

~~In general,~~ The difference between the ISRF data points and the ~~laser performed worse during the radiance measurements, yielding radiance ISRF measurements of poorer quality than the irradiance measurements. This can be seen in Fig. ??, which shows in general higher rms values for the ISRF fits for the radiance measurements~~ISRF model are very small, as the median of the rms is 0.0015 for both irradiance and radiance measurements, but the coverage of the first is much better. Therefore, the ~~radiance ISRF~~ smoothed ISRF derived from irradiance measurements are used ~~for validation of the SWIR~~ to generate the TROPOMI-SWIR ISRF calibration key data~~obtained using the irradiance ISRF measurements.~~. The ISRF model parameters are presented in Figs. 8–13. The skew-normal width parameter is sensitive to the photo-sensitivity of the SWIR detector (Fig. 6 of Hoogeveen et al., 2013). These patterns are easily recognizable in the residual plot (Fig. 8b), where the difference is shown between the ISRF parameter d and its bivariate poynomial fit.

~~For the comparison of the irradiance ISRF with the radiance ISRF, swath angles with the best spectral coverage and quality are selected.From the radiance and irradiance data the rows at ranges 40–72 and 110–140 are selected. Figure ?? shows the median of the~~ Figure 14 shows the differences between the smoothed ISRF and local ISRFs determined from irradiance, radiance and diode-laser measurements at the five locations presented in Figs. 3–5. The fit parameters are compared in Table 2.

The differences between the ISRF shape parameters as a function of column (before bivariate parameter fitting). In general, the spread in the irradiance data is larger. This is due to the fact that all irradiancedata of a column are taken in a single laser scan, while the radiance data of a column is taken from about 100 laser scans, thus averaging out some of the laser irregularities. The skew-normal width and block width show very good agreement at the right side of the detector, including the wiggles which are also visible in Fig. 5a. On the left side of the detector, the block width of the radiance ISRF tends to be smaller than that of the irradiance ISRF . This subtle difference is attributed to the non-optimal scanning of the laser at these wavelengths. The skew parameter tends to be slightly lower for the radiance measurements . However, the impact data points and the smoothed ISRF are for most measurements within the requirement on the ISRFof this difference is almost negligible. The tail parameters show reasonable resemblance in the two data sets, given the noise in both parameters.

In conclusion, the differences between the measured radiance and irradiance ISRFare too small to conclude that there is a significant difference between the two. More likely, differences are caused by imperfections of the laser-scan behavior or due to subtle differences in residual stray light. This justifies the use of the irradiance measurements . In general, all local ISRF fits with rms values less than 0.002 in Fig. 7 have also small residuals against the smoothed ISRF. Therefore, we conclude that smoothed ISRF, used to derive the ISRF calibration key data. Moreover, the radiance measurements effectively provide an independent validation of the derived ISRFs. CKD, agrees well with the local ISRF data.

5 In-flight Monitoring monitoring of ISRF

As knowledge of the ISRF is critical for the science results of the SWIR band, it has been decided to include means to monitor identify possible changes in the ISRF between the on-ground calibration campaign and the first measurements in space, and to monitor the ISRF stability during the 7 years of operational lifetime. For this, five tunable diode lasers in DFB diode lasers, spread evenly over the SWIR wavelength range, are included in the on-board calibration unit. Roughly once per month, the ISRF will be monitored using each laser. The laser wavelengths are scanned by tuning the temperature of the laser using a built-in thermo-electric cooler. The scanning range is about 6 spectral pixels so that the ISRF can be monitored for one or two wavelength pixels per laser. The Technical details of the on-board laser illuminates the SWIR spectrometer via a dedicated diffuser. As the diffuser is not moved during the measurements, there will be speckle.Most speckle is removed by taking the median of the data of all illuminated rows.

During the lasers are given in Sect. 2.1. During the in-flight commissioning phase, in-flight the on-ground measurements with the on-board lasers will be performed repeated with a moving and a fixed diffuser. The ISRF obtained from these measurements diffuser. Hence, these ISRFs can be comparedwith the ISRF measured on ground using the external laser and the on-board diode lasers to detect any possible changes. The early in-flight measurements also act as a reference "reference ISRF" for the ISRF monitoring. The monitoring ISRF is of sufficient quality to check for any degradation of the instrument but cannot be applied in

During the operational phase, dedicated measurements are planned to monitor ISRF stability. These measurements will be performed with each laser, roughly once per month with a fixed diffuser, because the diffuser mechanism is a life-limited item.

The ISRF determined from these measurements ("monitoring ISRF") is less accurate as it is affected by laser speckle patterns. It is used for monitoring only, not for trace-gas ~~retrieval. Should it be necessary, the~~ retrieval. If recalibration of the ISRF is necessary, then the wavelength scan of the on-board ~~diode lasers can be used to recalibrate the ISRF for a significant part of the SWIR band.~~

~~With an oscillating diffuser, the ISSF and pixel ISRF are determined in four stages, as described in Sect. 3, except that ISRF parameter smoothing (Sect. ??) is calculated from the ISRF fits of the few columns scanned per diode laser. The column dependence of the shape parameters is neglected and the row dependence is smoothed by a second order polynomial~~diode lasers has to be maximized and a moving diffuser should be used.

The monitoring ISRF ~~for each of the five lasers~~ is determined with the algorithm presented in Sect. 3 without iterations. It starts with the ISSF fit of stage 4 ~~where~~ using the parameters of a reference ISRF~~is used based on smoothed parameters of the given row. Thenthe median ISRF is~~, determined earlier in the mission with the same diode laser. Then, for each illuminated row, ISRF data of several spectral pixels are combined to generate one ISRF up to 5 pixels from its center. Speckle patterns are reduced by a median calculated from all ISRF data ~~of the central one/two fully-scanned columns, neglecting any row dependence.~~

~~The ISRF determination using the diode laser with and without moving on-board diffuser has been tried during the ground test and calibration campaigns. The ISRF measured with the diode lasers is in close agreement with the ISRF calibration data, thus proving the usability of the method and validating the calibration data. The monitoring ISRF deviates from the ISRF calibration data as could be expected. However, it is believed the~~ points. This monitoring ISRF will be compared with a monitoring ISRF obtained early in the commissioning phase and used in trend analyses. It is expected that this method is sensitive enough to be used ~~on board~~ for long-term monitoring, and being able to distinguish between changes in the real instrument ISRF and changes in the speckle pattern.

6 Conclusions

~~A new and accurate method~~ An approach is presented to determine high-resolution ISRFs for a spectrometer that measures the ISSF with only a few spectral pixels, using a scanning ~~OPO has been developed and applied to characterize the TROPOMI-SWIR ISRF.~~ monochromatic light source. The instrument itself is used to determine the wavelength and intensity of the light, which makes it possible to perform the necessary measurements within a reasonable time (days) even for detectors with more than 100,000 pixels.

The wavelength and intensity of the signal are determined with a fit to the measurements, but the model used for this ISSF fit is decisive for the accuracy of the ISRF determination, as is shown using simulations with synthetic ISRF data. Based on the simulations, an iterative approach is developed to improve the ISSF model from a simple model in the first iteration to the mirrored ISRF model in later iterations. The simulations show satisfactory convergence to the true ISRF in 4 iterations.

The ~~ISRF characterization has been performed on the basis of stray-light corrected irradiance measurements. The~~ TROPOMI-SWIR ISRF is modeled by the weighted sum of functions for the peak and the tails. The peak function is a skew-normal distribution

convolved with a ~~block distribution, and the tail function is a~~ uniform distribution. This corresponds to a (possibly asymmetric) image of the slit on the detector, with the optics blurring the image. For the tails a function is needed with an adjustable tail shape. A suitable function is the Pearson type VII distribution~~. An iterative scheme to derive the SWIR ISRF has been developed, where the ISRF determined in a previous iteration is used to improve the ISSF model in the current iteration. The required accuracy of the ISRF is obtained within 4 iterations~~, which is a generalization of the Gauss and Lorentz distributions. It can represent the wings of SWIR spectral stray light satisfactorily. Each of the five ISRF shape parameters ~~has been~~ are smoothed by fitting a bivariate ~~Chebyshev expansion~~ polynomial to derive the ISRF calibration key data for all SWIR wavelengths and swath angles.

The ISRF measured through the irradiance port using the solar diffuser has been compared with the equivalent ISRF measured via the radiance port. The differences ~~between the ISRFs derived from both data sets~~ are very small, and ~~largely due to differences in stray-light treatment and laser scan imperfections. The derived~~ are mostly due to measurement details, not instrument details. Calibration key data for the ISRF have been derived from the larger irradiance data set. The determined ISRF meets the requirement on ISRF knowledge and should thus be sufficient for ~~methane~~ SWIR trace-gas retrievals.

The on-board calibration unit contains five diode lasers in the SWIR wavelength range. ~~These diode lasers will be employed to verify~~ Accurate measurements with these diode lasers before and after launch will reveal whether the ISRF remained stable and the ISRF calibration key data ~~after launch~~can be applied for data retrieval. During operations, the lasers will be used to monitor the long-term stability of the optical properties of the SWIR module.

7 Data availability

The underlying data of the figures presented in this publication can be found at ftp://ftp.sron.nl/open-access-data/richardh.

Competing interests. The authors declare that they have no conflict of interest.

Acknowledgements. The authors would like to thank the teams of Airbus Defence and Space Netherlands and KNMI for organizing the calibration campaign and in particular the operators for the tireless data acquisition. The authors would also like to thank the anonymous referees for their thorough reviews of the original manuscript.

TROPOMI is a collaboration between Airbus Defence and Space Netherlands, KNMI, SRON and TNO, on behalf of NSO and ESA. Airbus Defence and Space Netherlands is the main contractor for the design, building and testing of the instrument. KNMI and SRON are the principal investigator institutes for the instrument. TROPOMI is funded by the following ministries of the Dutch government: the Ministry of Economic Affairs, the Ministry of Education, Culture and Science, and the Ministry of Infrastructure and the Environment.

References

Beers, T. C., Flynn, K., and Gebhardt, K.: Measures of Location and Scale for Velocities in Clusters of Galaxies—A Robust Approach, The Astronomical Journal, 100, 32–46, https://doi.org/10.1086/115487, 1990.

Beirle, S., Lampel, J., Lerot, C., Sihler, H., and Wagner, T.: Parameterizing the instrument spectral response function and its changes by a super-Gaussian and its derivatives, Atmos. Meas. Tech., 10, 581–598, https://doi.org/10.5194/amt-10-581-2017, 2017.

Buscaglione, F.: GMES Sentinel-5 Precursor — S5p System Requirement Document (SRD), S5p-RS-ESA-SY-0002, ESA, issue 4.1, 2011.

Day, J. O., O'Dell, C. W., Pollock, R., Bruegge, C. J., Rider, D., Crisp, D., and Miller, C. E.: Preflight Spectral Calibration of the Orbiting Carbon Observatory, IEEE Transactions on Geoscience and Remote Sensing, 49, 2793–2801, https://doi.org/10.1109/TGRS.2011.2107745, 2011.

Dobber, M. R., Dirksen, R. J., Levelt, P. F., van den Oord, G. H. J., Voors, R. H. M., Kleipool, Q., Jaross, G., Kowalewski, M., Hilsenrath, E., Leppelmeier, G. W., de Vries, J., Dierssen, W., and Rozemeijer, N. C.: Ozone Monitoring Instrument Calibration, IEEE Transactions on Geoscience and Remote Sensing, 44, 1209–1238, https://doi.org/10.1109/TGRS.2006.869987, 2006.

Hoogeveen, R. W. M., Voors, R., Robbins, M. S., Tol, P. J. J., and Ivanov, T. I.: Characterization results of the TROPOMI Short Wave InfraRed detector, Proceedings of SPIE, 8889, 888–913, https://doi.org/10.1117/12.2028759, 2013.

Hu, H., Hasekamp, O., Butz, A., Galli, A., Landgraf, J., aan de Brugh, J., Borsdorff, T., Scheepmaker, R., and Aben, I.: The operational methane retrieval algorithm for TROPOMI, AMT, 9, 5423–5440, 2016.

Kleipool, Q., Babić, L., Bartstra, R., Braak, R., Dierssen, W., Dewitte, P.-J., Kenter, P., Leloux, J., Loots, E., Ludewig, A., Meijering, P., van der Plas, E., Rozemeijer, N., Schepers, D., Schiavini, D., Smeets, J., Vacanti, G., and Vonk, F.: Pre-launch calibration status of the TROPOMI payload on-board the Sentinel 5 precursor satellite, submitted to Atmos. Meas. Tech., 2018.

Patefield, M. and Tandy, D.: Fast and Accurate Calculation of Owen's T Function, Journal of Statistical Software, 5, 1–25, http://people.sc.fsu.edu/~jburkardt/f_src/owens/owens.html, 2000.

Schrijver, H., Gloudemans, A. M. S., Frankenberg, C., and Aben, .: Water vapour total columns from SCIAMACHY spectra in the 2.36 μm window, Atmos. Meas. Tech., 2, 561–571, 2009.

Sun, K., Liu, X., Nowlan, C. R., Cai, Z., Chance, K., Frankenberg, C., Lee, R. A. M., Pollock, R., Rosenberg, R., and Crisp, D.: Characterization of the OCO-2 instrument line shape functions using on-orbit solar measurements, Atmos. Meas. Tech., 10, 939–953, https://doi.org/10.5194/amt-10-939-2017, 2017.

Tol, P. J. J., van Kempen, T. A., van Hees, R. M., Krijger, M., Cadot, S., Aben, I., Persijn, S. T., and Hoogeveen, R. W. M.: Characterization and correction of stray light in TROPOMI-SWIR, submitted to Atmos. Meas. Tech., 2018.

van Amerongen, A., Krol, H., Grèzes-Besset, C., Coppens, T., Bhatti, I., Lobb, D., Hardenbol, B., and Hoogeveen, R. W. M.: State of the art in silicon immersed gratings for space, Proceedings of the International Conference on Space Optics, 2012.

Veefkind, J. P., Aben, I., McMullan, K., Förster, H., De Vries, J., Otter, G., Claas, J., Eskes, H. J., De Haan, J. F., Kleipool, Q., van Weele, M., Hasekamp, O., Hoogeveen, R. W. M., Landgraf, J., Snel, R., Tol, P., Ingmann, P., Voors, R., Kruizinga, B., Vink, R., Visser, H., and Levelt, P. F.: TROPOMI on the ESA Sentinel-5 Precursor: A GMES mission for global observations of the atmospheric composition for climate, air quality and ozone layer applications, Remote Sensing of Environment, 120, 70–83, https://doi.org/10.1016/j.rse.2011.09.027, 2012.

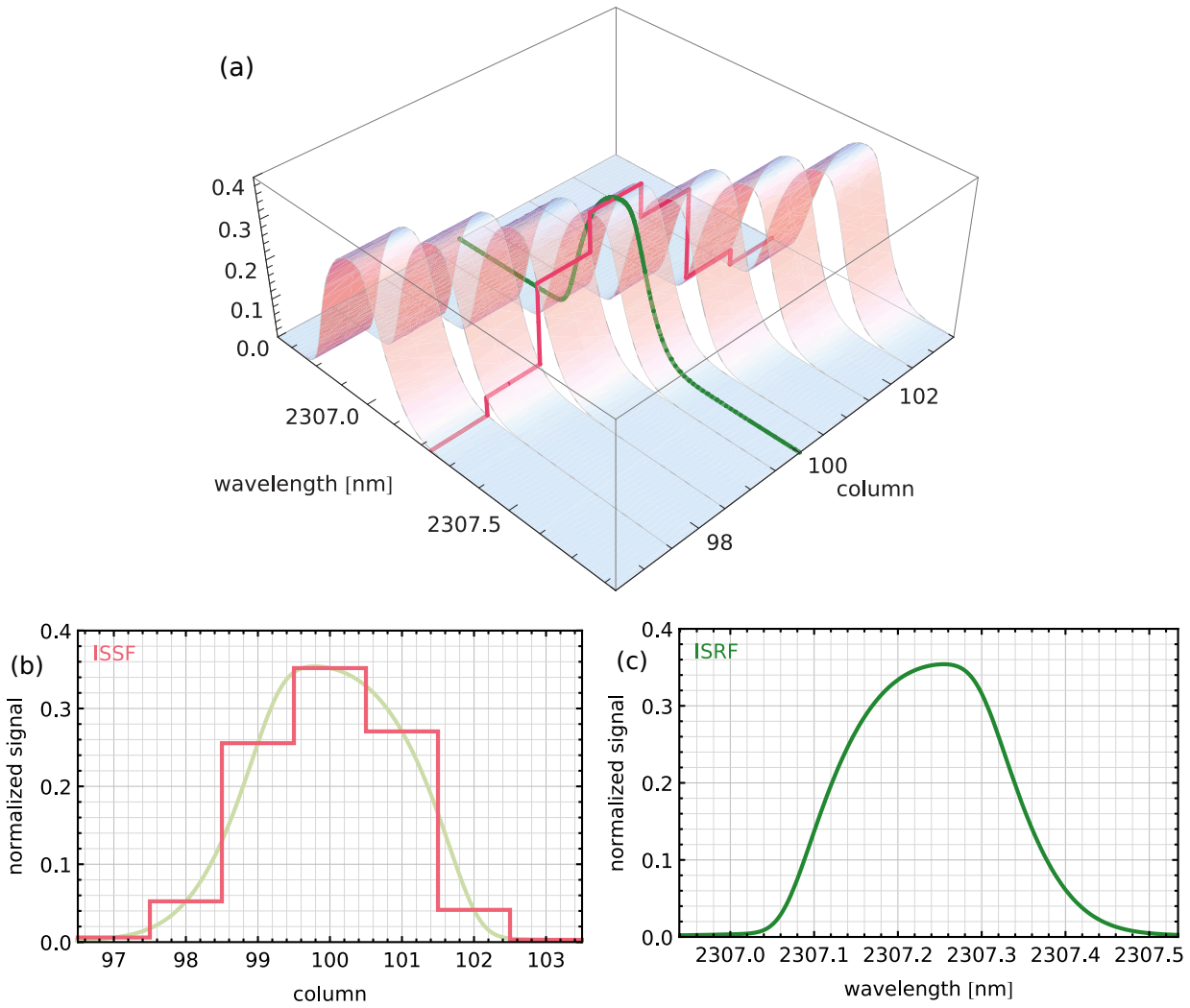

Figure 1. Normalized signal as a function of source wavelength and pixel on an arbitrary row, with two cross sections: the ISSF at 2307.24 nm (red) and the ISRF of the pixel in column 100 (green). In the plot of the ISSF, a mirrored version of the ISRF is shown in light green. The skew of the ISRF has been exaggerated to show the mirroring.

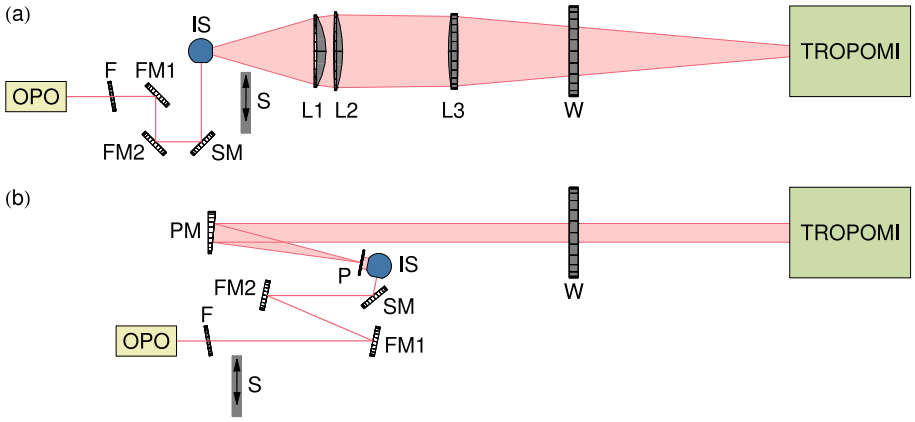

Figure 2. ~~Convergence of the ISRF model towards a synthetic ISRF using the ISRF parameter iteration.~~ The ~~results~~ setup for ~~the 'skewed' synthetic ISRF are shown in panels~~ (a) irradiance measurements and (b) ~~, where panel (a) shows the relative difference between~~ radiance measurements. The elements after the ~~ISRF data~~ OPO are: neutral density filter F, folding mirrors FM1 and ~~the ISRF fit~~FM2, spinning mirror SM, integrating sphere IS, shutter S, lenses L1, L2 and ~~panel (b) shows the relative difference between the ISRF fit~~ L3, field stop P, parabolic mirror PM and window W of the ~~'true' ISRF~~vacuum chamber containing TROPOMI. ~~Panel~~ The light enters (~~e~~a) ~~and~~ the Sun port or (~~d~~b) ~~show~~ the ~~results for~~ Earth port of the ~~'symmetric' synthetic ISRF~~instrument.

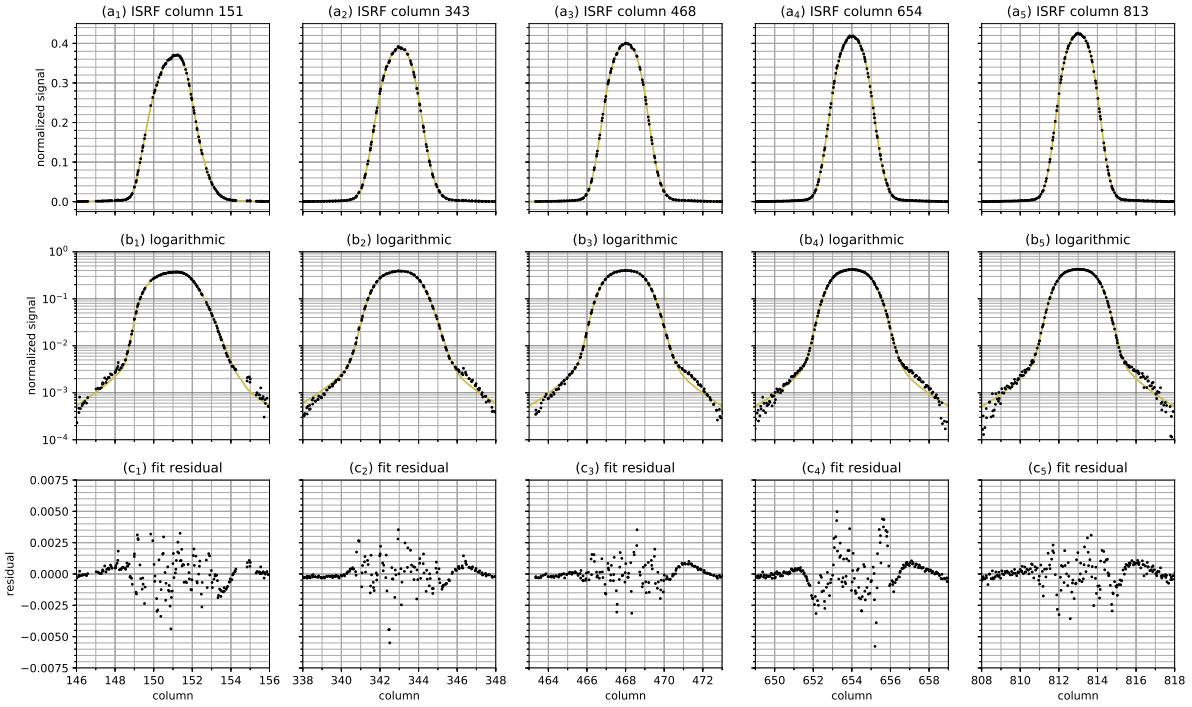

Figure 3. ~~Examples of~~ Five typical SWIR ISRFs determined from on-ground measurements with an external laser through the ~~median~~ TROPOMI irradiance ~~ISRF data with fits~~port. The ~~ISRF fit parameter values~~ upper panels (a) show the shapes of the ~~columns 128, 300, 540, 726 and 935 are respectively~~ISRF at location: ~~(skew-normal width) 0.575, 0.509, 0.444, 0.432 and 0.425; (skew) 2.880~~columns 151, ~~2.062~~343, ~~0.825~~468, ~~0.334~~ 654 and ~~-0.689; (block width) 2.669, 2.594~~813, ~~2.461~~resp., ~~2.388~~ and ~~2.301; (tail fraction) 0.081~~rows 24, ~~0.108~~76, ~~0.101~~118, ~~0.103~~ 155 and ~~0.097; (tail shape) 1.25; (tail width) 1.158, 0.988, 0.972~~191, ~~0.952 and 1.010~~resp. The ~~plots~~ middle panels (b) show the same data ~~and fits~~ on a ~~linear (top) and~~ logarithmic ~~(middle)~~ scale. The ~~residuals are shown in~~ lower panels (c) show the ~~bottom plots~~difference between the ISRF data points and the ISRF fit (end of stage 4).

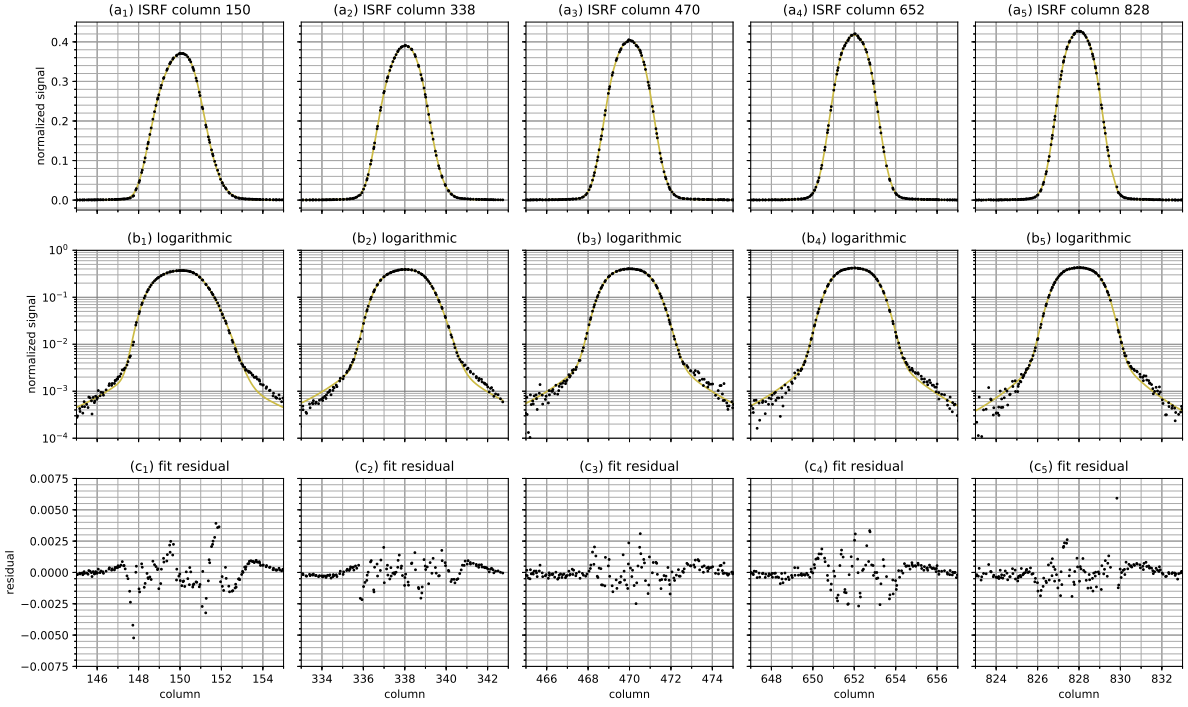

Figure 4. ~~As in Fig. **??**, for radiance~~ Five typical SWIR ISRFs determined from on-ground measurements with an external laser through the TROPOMI radiance port. The ~~ISRF fit parameter values~~ upper panels (a) show the shapes of the ISRF at location: columns ~~128~~150, ~~300~~338, ~~540~~471, ~~726~~ 652 and ~~935 are respectively: (skew-normal width) 0.620, 0.527~~828, ~~0.444~~resp., ~~0.445~~ and ~~0.451; (skew) 2.569~~rows 24, ~~1.650~~76, ~~0.786~~118, ~~-0.701~~ 155 and ~~-0.879; (block width) 2.641, 2.607, 2.452~~191, ~~2.363 and 2.307;~~ resp. The middle panels (~~tail fraction~~b) ~~0.079, 0.108, 0.110, 0.100 and 0.106;~~ show the same data on a logarithmic scale. The lower panels (~~tail shape~~c) ~~1.65;~~ show the difference between the ISRF data points and the ISRF fit (~~tail width~~end of stage 4)~~1.625, 1.238, 1.142, 1.235 and 1.196~~.

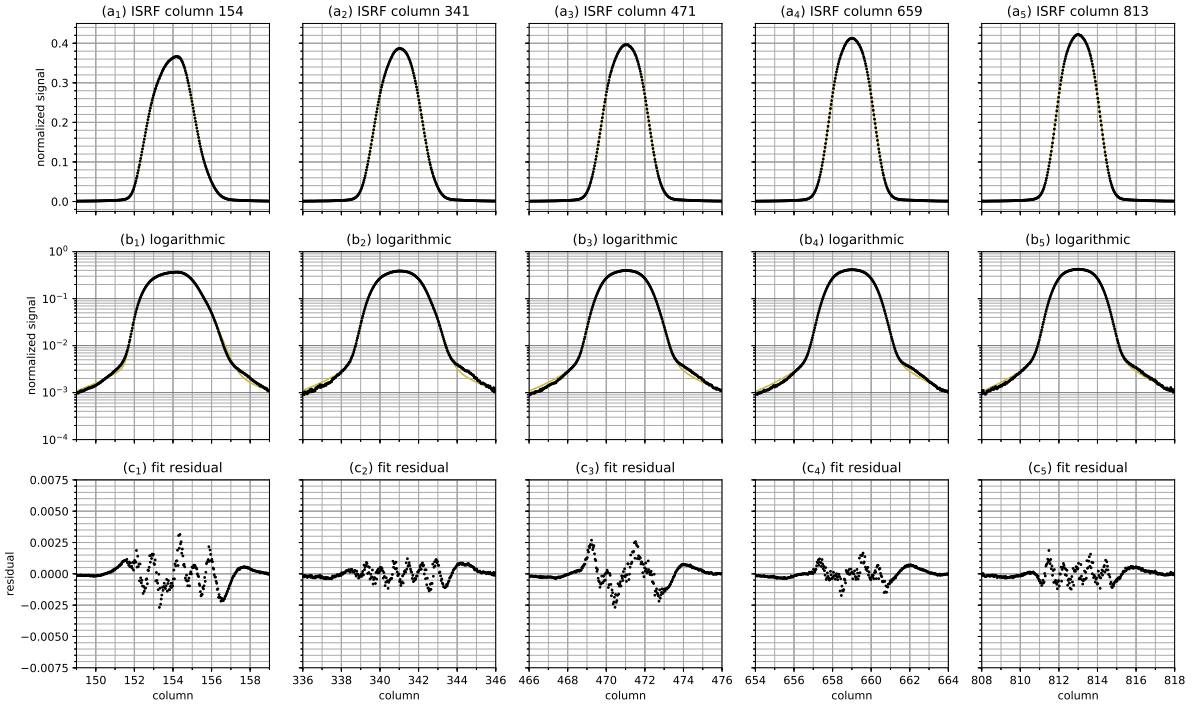

Figure 5. SWIR ISRF determined from on-ground measurements with the five on-board diode lasers. The upper panels (a) show the shapes of the ISRF at location: columns 154, 341, 471, 659 and 813, resp., and rows 24, 76, 118, 155 and 191, resp. The middle panels (b) show the same data on a logarithmic scale. The lower panels (c) show the difference between the ISRF data points and the ISRF fit (end of stage 4).

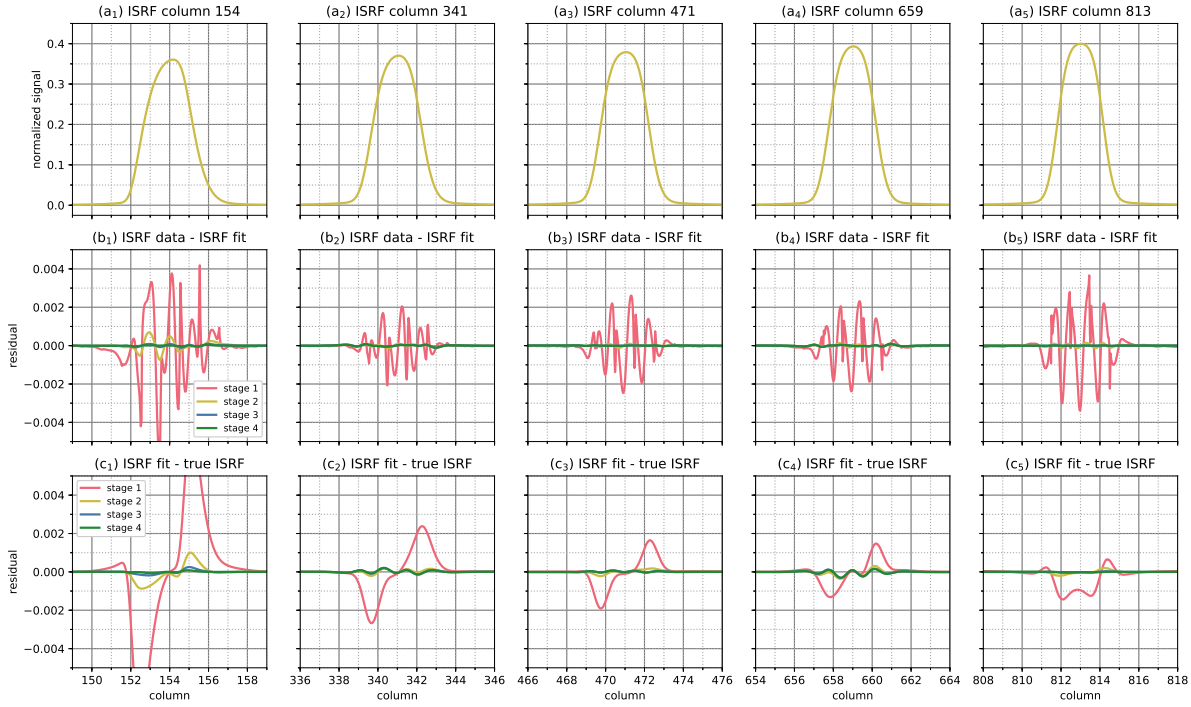

Figure 6. Convergence of five synthetic ISRF determinations in four stages. The upper panels (a) show the shapes of synthetic ISRF closely resemble the ISRF examples as shown in Figs. 3–5. The middle panels (b) show the difference between the ISRF data points and the ISRF fit. The lower panels (c) show the difference between the ISRF data points and the true ISRF.

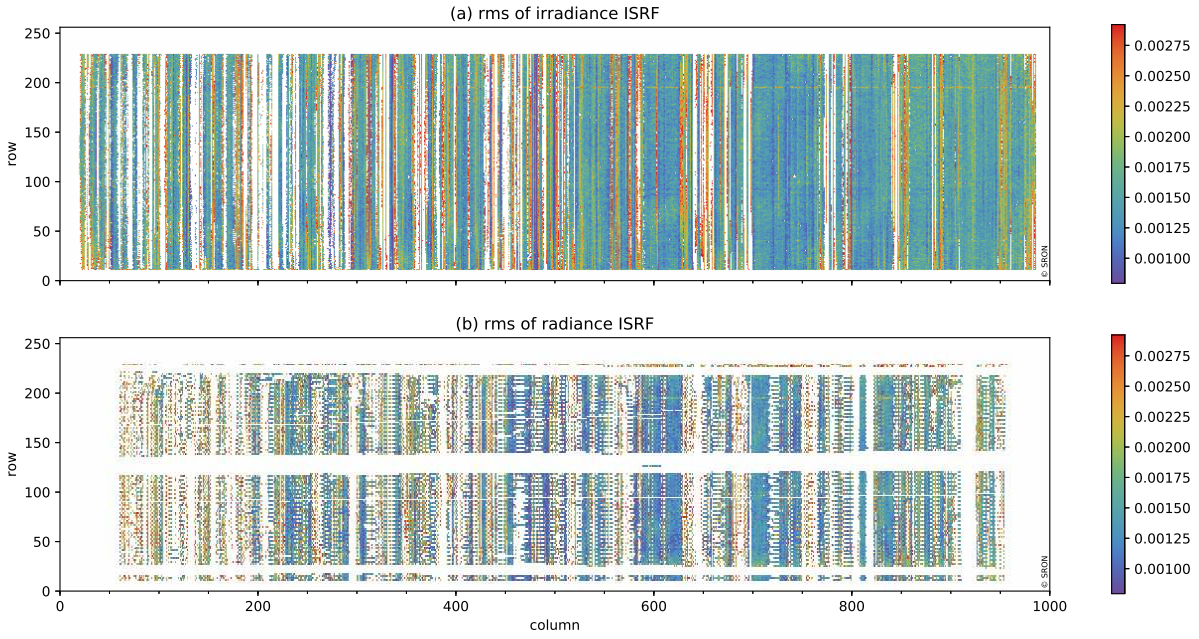

Figure 7. Fit quality of the local ISRF using the (a) irradiance port and (b) radiance port. No measurements are performed in the white edges. Panel (a) white vertical stripes are due to saturation in the measurements, and red vertical stripes are due to nearby saturation or laser instabilities. Panel (b) white areas are due to partly illuminated rows.

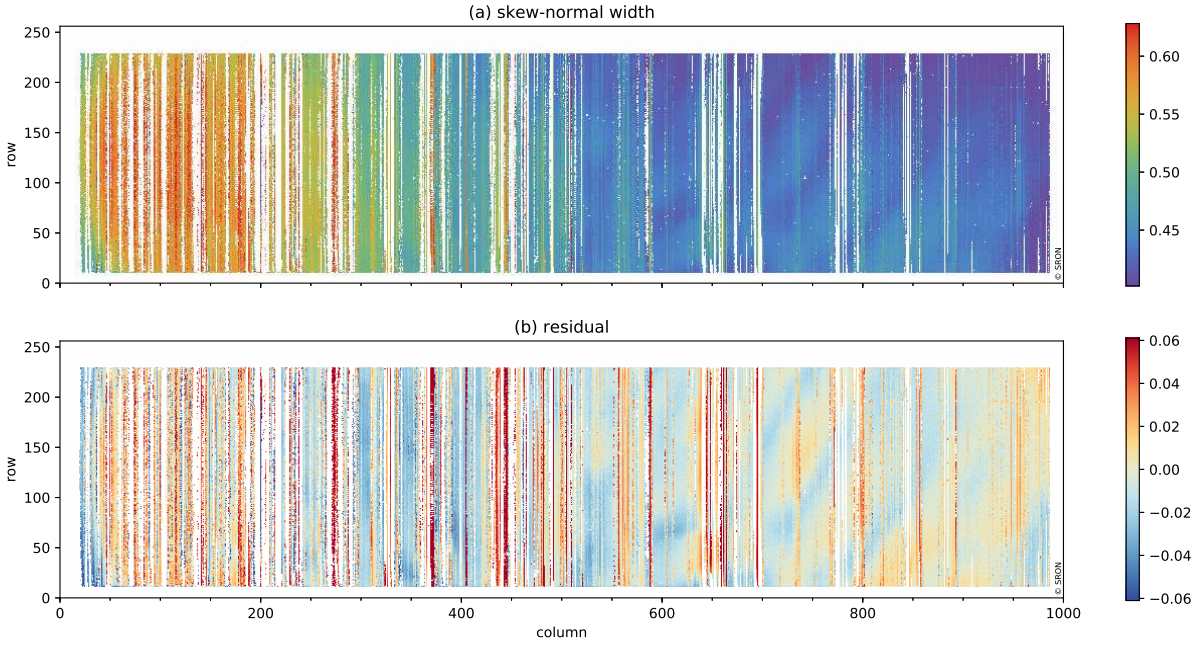

Figure 8. ~~Irradiance~~ ISRF ~~fit results for the peak function (final):~~ parameter skew-normal width d ~~. Presented are (a) ISRF fit, (~~irradiance port)~~ISRF parameter fit, and ~~. Panel (b) shows the difference between the two~~d and its bivariate poynomial fit. ~~In~~ No measurements are performed in the white ~~area, the ISRF fit failed (~~edges. White vertical stripes ~~), the light is blocked by the entrance slit of the spectrometer (top and bottom) or a shield at~~ are due to saturation in the ~~detector (left and right)~~measurements. ~~The white spots~~ Red vertical stripes are ~~bad pixels~~due to nearby saturation or laser instabilities.

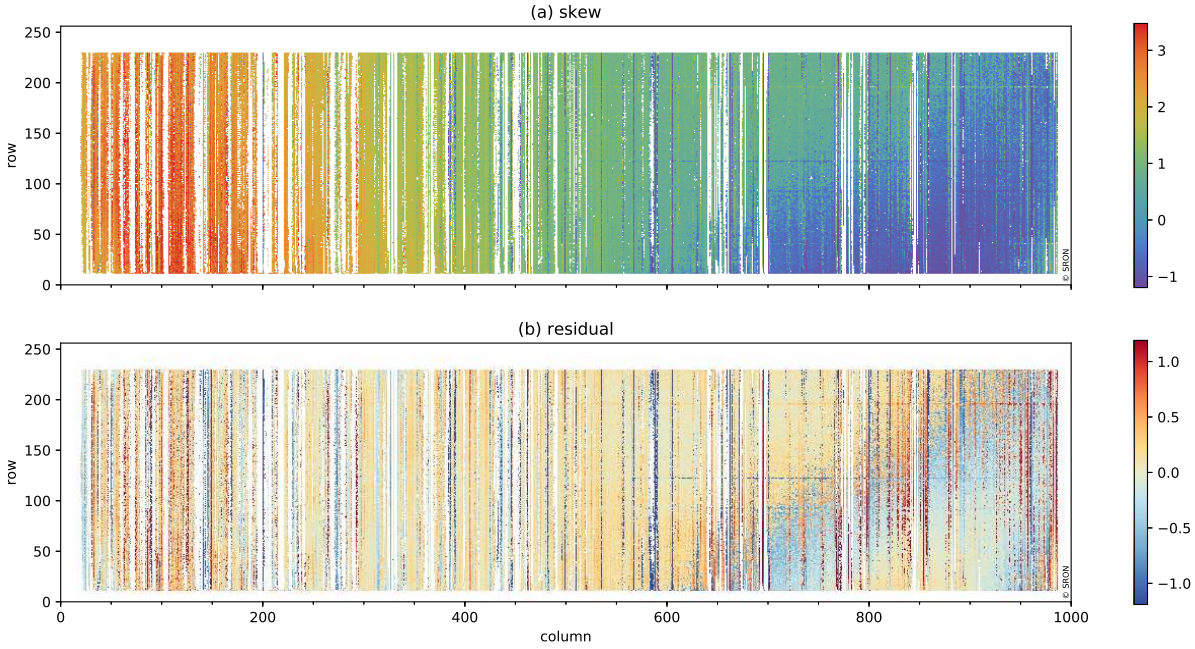

Figure 9. ~~Irradiance~~ ISRF ~~fit results:~~ parameter skew *s* (airradiance port)~~quality of ISRF fit and~~ . Panel (b) ~~quality of ISRF parameter fit, based on~~ shows the ~~rms value. The threshold between good and moderate is 0.004 and~~ difference between ~~moderate~~ *s* and ~~bad 0.0065~~its bivariate poynomial fit. ~~In the gray area, the light is blocked by~~ No measurements are performed in the ~~entrance slit of~~ white edges. White vertical stripes are due to saturation in the ~~spectrometer (top and bottom)~~ measurements. Red vertical stripes are due to nearby saturation or ~~by the shield at the detector (left and right)~~laser instabilities.

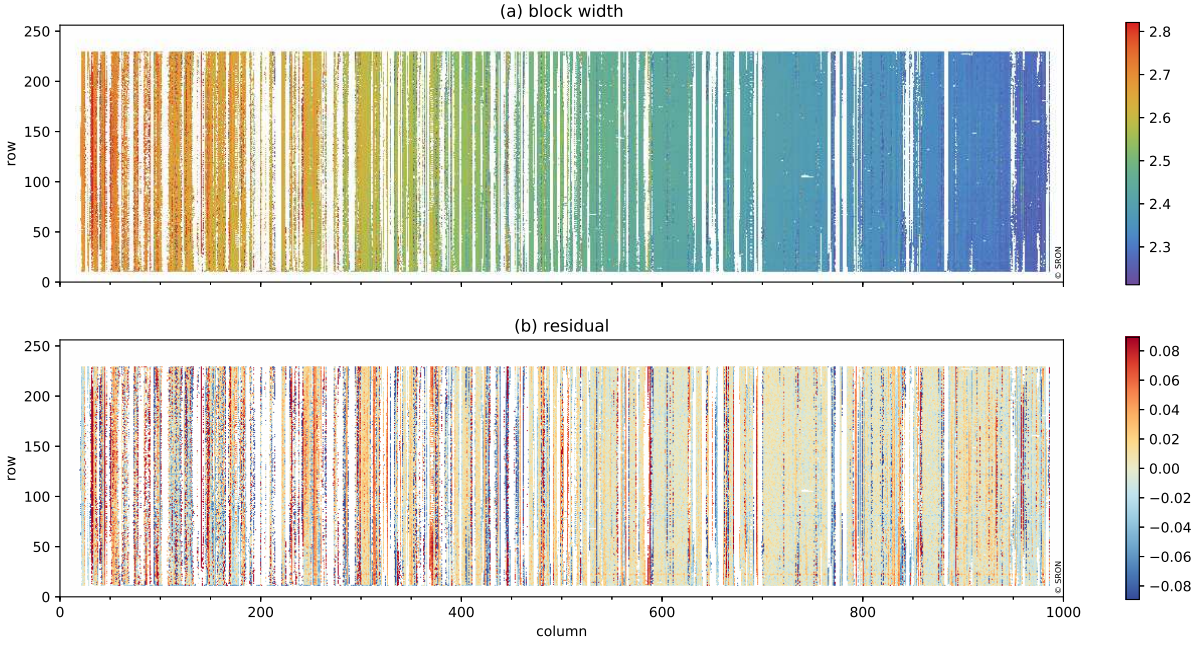

Figure 10. ~~Same as Fig~~ISRF parameter block width w (irradiance port). ~~**??, except for**~~ Panel (b) shows the ~~radiance ISRF~~difference between w and its bivariate poynomial fit. No measurements are performed in the white edges. White vertical stripes are due to saturation in the measurements. Red vertical stripes are due to nearby saturation or laser instabilities.

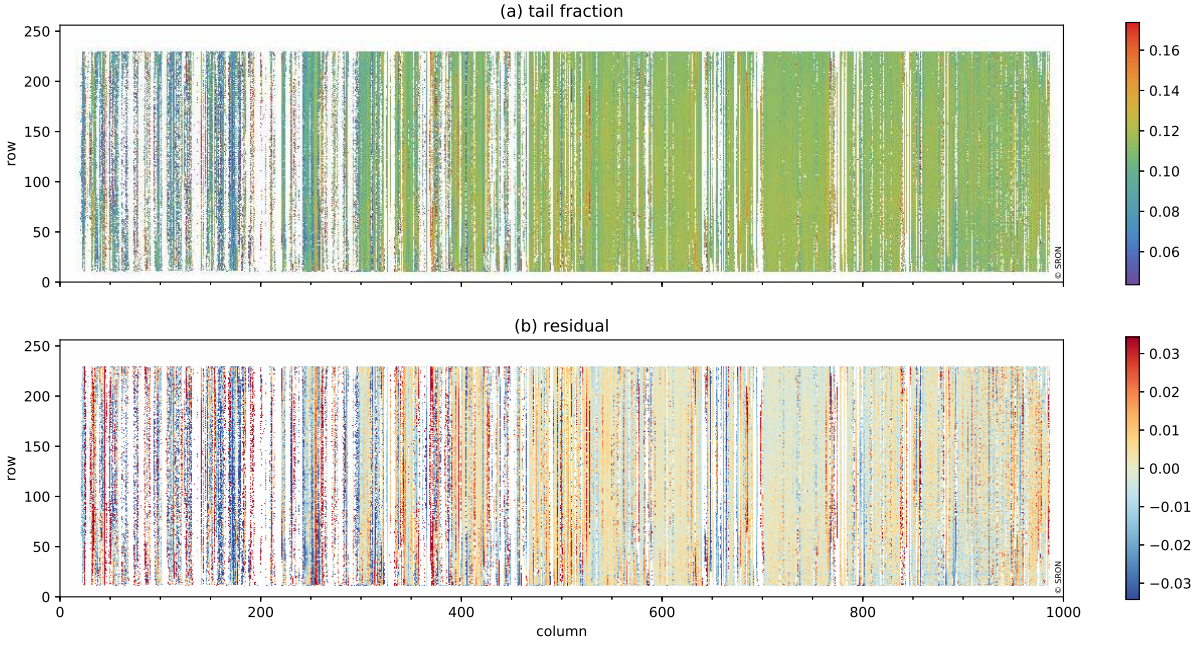

Figure 11. ~~Comparison of the five~~ ISRF ~~parameters derived from~~ parameter tail fraction η (irradiance port). Panel (b) shows the difference between η and ~~radiance~~ its bivariate poynomial fit. No measurements ~~: as a function of column~~are performed in the white edges. White vertical stripes are due to saturation in the measurements. Red vertical stripes are due to nearby saturation or laser instabilities.

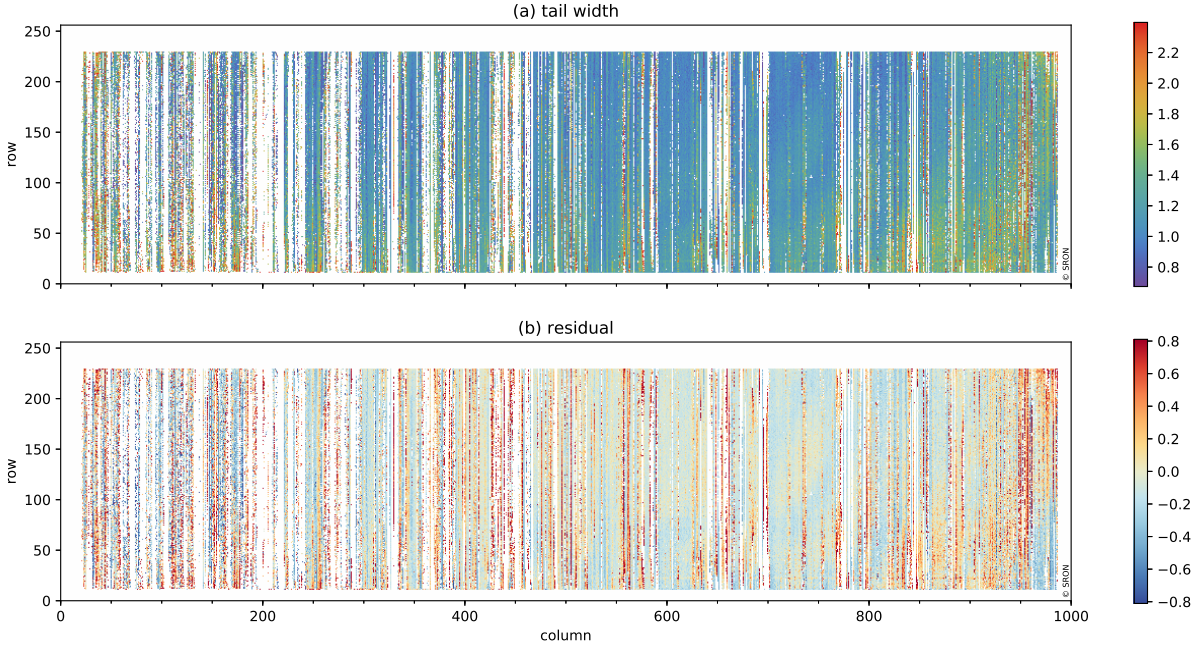

Figure 12. ISRF tail parameter γ (irradiance port). Panel (b) shows the difference between γ and its bivariate poynomial fit. No measurements are performed in the white edges. White vertical stripes are due to saturation in the measurements. Red vertical stripes are due to nearby saturation or laser instabilities.

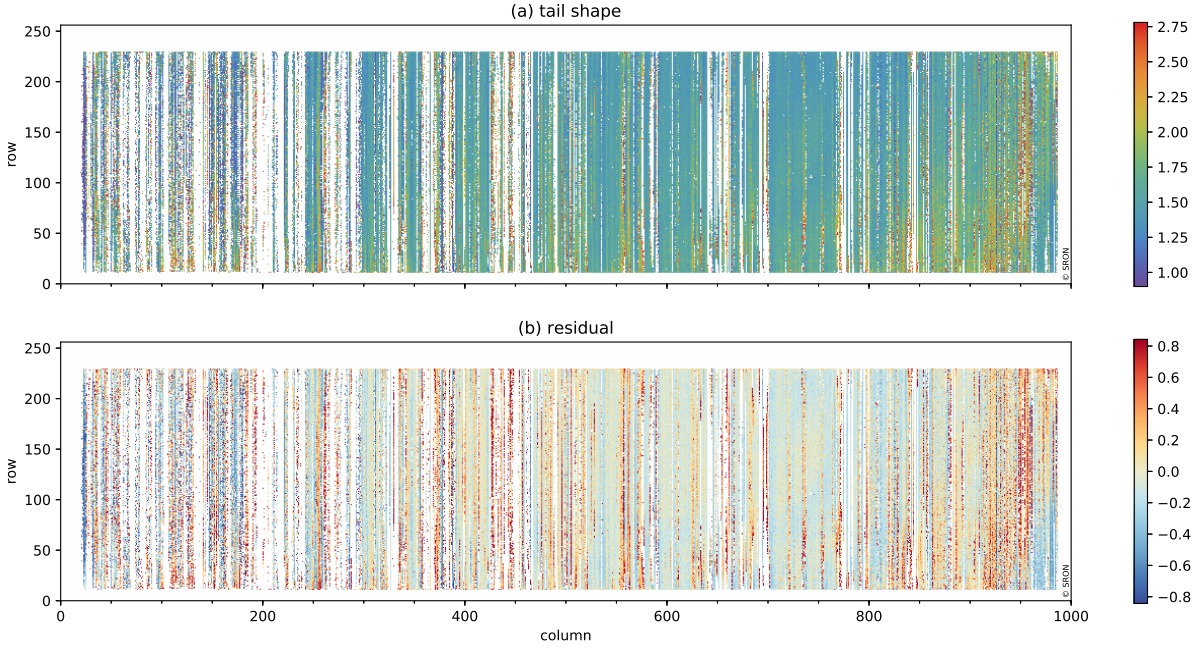

Figure 13. ISRF tail parameter m (irradiance port). Panel (b) shows the difference between m and its bivariate poynomial fit. No measurements are performed in the white edges. White vertical stripes are due to saturation in the measurements. Red vertical stripes are due to nearby saturation or laser instabilities.

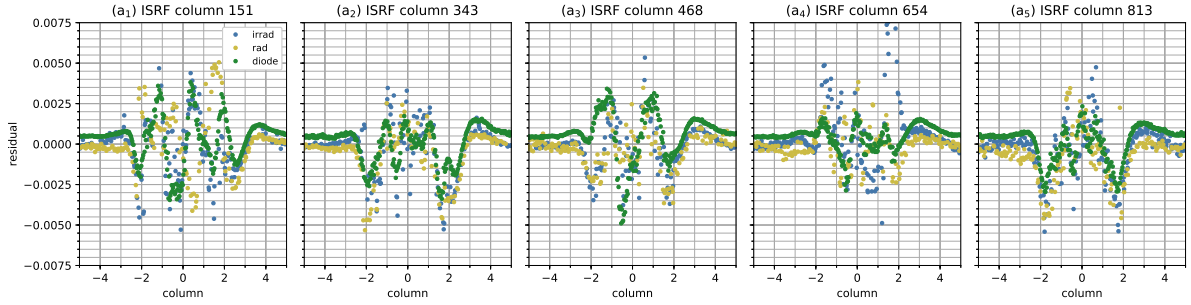

Figure 14. Differences between the local ISRF and the smoothed ISRF for irradiance, radiance and diode-laser measurements. This figure illustrates that smoothed ISRF data agree well with the local ISRF data presented in Figs. 3–5.

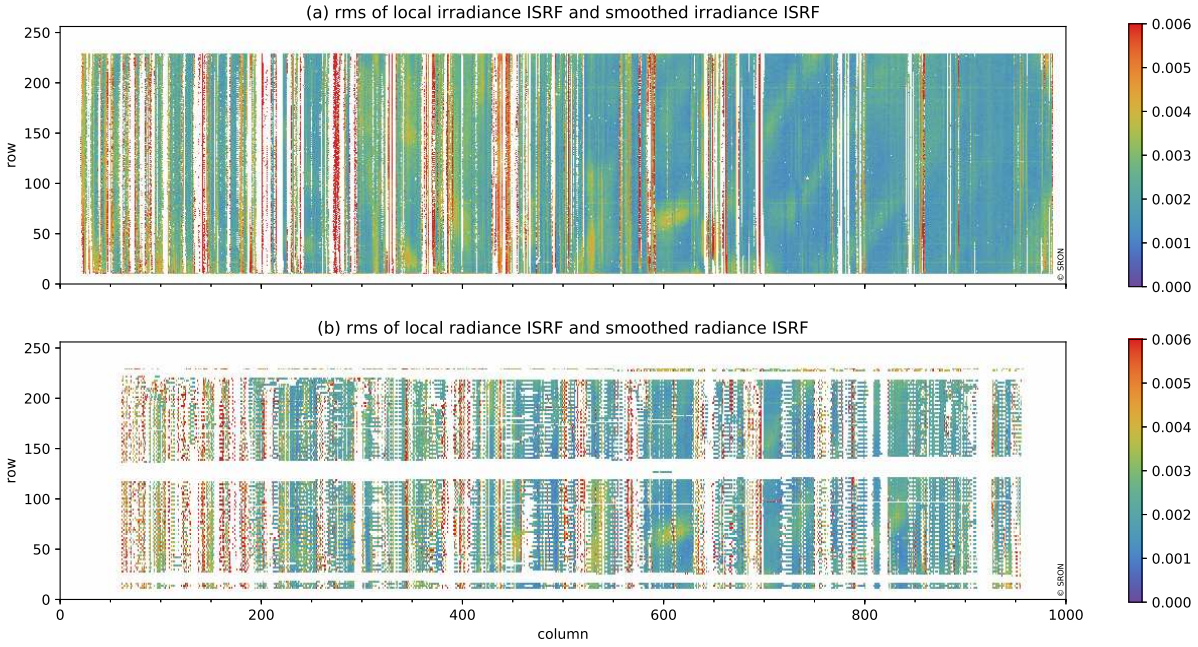

Figure 15. Fit quality of the smoothed ISRF using the (a) irradiance port and (b) radiance port. No measurements are performed in the white edges. Panel (a) white vertical stripes are due to saturation in the measurements, and red vertical stripes are due to nearby saturation or laser instabilities. Panel (b) white areas are due to partly illuminated rows.

Table 1. ~~Treatment of parameters in each stage and for each type~~ The convergence of ~~data set: either hold constant (entry is a number), interpolate~~ the ~~previous~~ ISRF ~~results (entry 'model') or include in~~ parameter iteration is shown by listing the ~~fit (entry 'fit'). In~~ determined ISRF parameters at the ~~case~~ end of ~~s~~ four stages. The simulations are performed on five synthetic ISRFs representative for ~~ISSF fits,~~ the ~~interpolated value is given the opposite sign~~determined TROPOMI-SWIR ISRF, equally spaced at positions on the SWIR detector from top left to ~~take into account that an ISSF is basically~~ bottom right. The synthetic data are generated without noise. The shape parameters for the ~~mirrored version of an~~ true ISRF are listed in italic.

~~stage data~~
(47, 15
~~2~~
(79, 34
~~4~~ (118, 4
~~Listing the intermediate parameters of the derived ISRF from two synthetic ISRF data sets: 'skew' and 'symmetric'. The ISRF parameter iteration is per~~
~~skew~~ (155
~~symmetric~~ (1

Table 2. Summary Listing of the irradiance ISRF characterizationparameters (Eq.Listed are for the 4 stages: the quality of the ISRF fit, the average and uncertainty over the complete array 13) of the rms, d, s, $w$five typical SWIR ISRFs determined from irradiance (irr), η radiance (rad) and γdiode-laser (ld) measurements, and the residuals between these parameter values and the parameter fitsrespectively. To avoid the effect The location of outliers, the biweight estimate of location and scale ISRF are used for (approximately) equally spaced at positions on the average and uncertainty, respectively (Beers et al., 1990)SWIR detector from top left to bottom right.

fit parameter pixel	type	stage 1 d	stage 2 s	stage 3 w	stage 4
quality (47, 151)	good irr	142409 0.5573	164012 3.3047	164646 2.66357	160161 0
(47, 150)	moderate rad	53253 0.5771	35639 2.2230	35118 2.67038	36560 0.
(47, 154)	bad ld	13296 0.5681	9907 3.1603	9604 2.64913	12946 0.
(79, 343)	failed irr	2617 0.4923	2015 1.4446	2206 2.57038	1907 0.1
rms 10^{-3} (79, 338)	median rad	3.15 ± 1.68 0.4941	2.44 ± 1.41 1.5636	2.41 ± 1.40 2.58129	2.53 ± 1.49
skew-normal width d (79, 341)	median ld	0.479 ± 0.058 0.4961	0.473 ± 0.060 1.6075	0.470 ± 0.060 2.58128	0.471 ± 0.05
(118, 468)	residual irr	-0.003 ± 0.028 0.4539	-0.004 ± 0.025 1.2030	-0.004 ± 0.025 2.51046	-0.005 ± 0.0
skew s (118, 470)	median rad	0.940 ± 1.164 0.4558	1.005 ± 1.204 1.0764	1.018 ± 1.207 2.50779	1.019 ± 1.18
(118, 471)	residual ld	0.018 ± 0.490 0.4561	0.017 ± 0.442 1.2055	0.012 ± 0.439 2.52954	0.010 ± 0.41
block width w (155, 654)	median irr	2.484 ± 0.176 0.4569	2.494 ± 0.168 1.0076	2.501 ± 0.166 2.42063	—0.10
(155, 652)	residual rad	-0.003 ± 0.052 0.4341	-0.004 ± 0.049 0.5962	-0.003 ± 0.049 2.42946	—0.10
tail fraction η (155, 659)	median ld	0.075 ± 0.029 0.4330	0.087 ± 0.029 0.7617	0.092 ± 0.029 2.42022	0.097 ± 0.01
(191, 813)	residual irr	-0.001 ± 0.029 0.4122	-0.001 ± 0.029 0.7598	-0.001 ± 0.029 2.36538	-0.001 ± 0.0
tail width γ (191, 828)	median rad	1.240 ± 0.562 0.4142	1.048 ± 0.321 0.3014	1.004 ± 0.255 2.35932	0.988 ± 0.13
(191, 813)	residual ld	0.231 ± 0.558 0.4168	0.066 ± 0.298 0.6230	0.040 ± 0.218 2.36022	0.009 ± 0.10

Irradiance ISRF fit results for the peak function (final): skew s. Presented are (a) ISRF fit and (b) ISRF parameter fit, see also Fig. 8.

Same as Fig. 9, except for block width w.

Same as Fig. 9, except for tail fraction η.

Same as Fig. 9, except for tail width γ.